AN EXAMINATION OF HYDROGEN FUEL CELLS AND LITHIUM-ION BATTERIES FOR ELECTRIC VERTICAL TAKE-OFF AND LANDING (EVTOL) AIRCRAFT

Wanyi Ng, wanyi.w.ng@gmail.com, University of Maryland in College Park (USA)
Anubhav Datta, datta@umd.edu, University of Maryland in College Park (USA)

Abstract

The primary drawback of electric vertical take-off and landing (eVTOL) aircraft is their poor range and endurance with practical payloads. The objective of this paper is to examine the use of hydrogen fuel cells to overcome this drawback through simulation and hardware testing. The paper develops steady state and transient models of fuel cells and batteries and validates the models experimentally. An equivalent circuit network model was able to capture the waveforms and magnitudes of voltage as a function of current, temperature, and humidity. Examination of the results revealed that the transient behavior of batteries and fuel stacks are significant primarily shortly after startup of the fuel stack and at the limiting ranges of high and low power; for a nominal operating power and barring faults, steady state models were adequate. This paper also demonstrates fuel cell and battery power sharing capabilities in an unregulated parallel configuration as well as in a regulated circuit. A regulating architecture was developed that achieved a reduction in power plant weight. Finally, the paper outlines weight models of motors, batteries, and fuel cells needed for eVTOL sizing, and carries out sizing analysis for three progressively longer on-demand urban air taxi missions. The objective aircraft was sized to carry a minimum of 400 lb payload for an on-demand air taxi-like mission with 5 min hover and 15-60 min cruise at 150 mph. This revealed that for ranges within 75 mi, an all-electric tilting proprotor configuration is feasible with current technology if high C-rate batteries are available. Either a battery-only or fuel cell and battery hybrid power plant is ideal, depending on the range of the mission. In particular, a 5700 lb gross take-off weight aircraft with disk loading of 11 lb/ft^2 could be sized using a hybrid power plant with fuel cells and 10C batteries to carry a payload of 430 lb for a 75 mi (inter-city) mission. A smaller aircraft of 4000 lb gross weight and a disk loading of 27 lb/ft^2 could be sized using a 6C battery only power plant to carry a payload of 490 lb for a shorter 38 mi (intra-city) mission. Research priorities would depend on target mission duration and range. For any mission beyond 40 miles (or 15 minutes at 150 mph) fuel cells appear to be a compelling candidate. Based simply on performance numbers (cutting-edge numbers proven at a component level but not in flight), ease of re-fueling, high w% hydrogen storage due to the short duration of eVTOL missions, and lack of a compressor due to low-altitude missions, fuel cells appear to far surpass any realistic future projections of Li-ion energy levels. However, for missions less than 40 miles, improving battery energy density is the priority. All mission lengths require improved battery power density to 6-10 C for 150 Wh/kg batteries.

1. INTRODUCTION

Recent advances in electrochemical power and electric motors have caused a significant resurgence of interest in manned electric vertical take-off and landing (eVTOL) aircraft[1]. Developers ranging from start-ups to major aerospace corporations have introduced many manned eVTOL concepts in various stages of development, since the world's first electric manned helicopter flight by TETRAERO in 2011[2] and the first multirotor flight by e-volo's Volocopter in 2012[3]. Electric power offers agile, quiet, safe, non-polluting, and potentially autonomous aircraft, which are essential characteristics for a new on-demand urban air transportation system. In 2017, Uber released a vision for such a system in a white paper[4]. The main drawback of these potential aircraft is the poor range and endurance with practical payload – at least 300-400 lb for a 2-3 seat aircraft. This drawback stems from the weight of lithium-ion batteries. The objective of this paper is to examine the use of hydrogen fuel cells to overcome this drawback.

A major limitation for battery powered electric aircraft is the energy density of batteries – 250 Wh/kg for lithium-ion cells and 170 Wh/kg for packs[6] – which is much lower than hydrocarbon fuels. Proton exchange membrane (PEM) fuel cells offer a higher energy density than batteries, around 500 Wh/kg, in a unit that is still clean and hydrocarbon free, mechanically simple, operates near ambient temperature, and produces no harmful emissions. Hybridization combines the high specific power of batteries with the high specific energy of fuel cells to optimize the system weight, while introducing redundancy in the power source for added safety.

Fuel cell and battery hybrid systems have been demonstrated in manned fixed-wing aircraft. The Boeing Fuel Cell Demonstrator achieved manned flight in 2008 with a gross weight of 870 kg for approximately 45 min[7]. The German Aerospace Center's electric motor glider Antares DLR-H2 has been used as a flying test-bed with a gross take-off weight of 825 kg[8,9,10]. This aircraft has been used to investigate different hybridization architectures to allow charging and minimize the power plant weight, as well as investigating methods to increase reliability. The ENFICA-FC project, funded by the European Commission and based at Politecnico di Torino, also developed a two-seater hybrid aircraft that achieved an endurance of 40 minutes[11]. These aircraft serve as a proof of concept for fuel cell powered flight, provide flight data, and identify key obstacles compared to conventional aircraft.

However, all of the above are fixed-wing, not rotary-wing, aircraft. eVTOL requires rotary-wing aircraft, which have unique challenges associated with rotor dynamics, lower lift to drag ratios (due to hub drag), and highly transient power requirements over a wider range of power magnitudes. Some unmanned rotary-wing aircraft have been flown using a fuel cell and battery hybrid power system, but these are smaller scale drones and little public data is available compared to the fixed-wing aircraft described previously. These rotary-wing aircraft include the United Technologies Research Center's 1-2 kW single main rotor helicopter in 2009[12] and EnergyOr's 10.5 kg quadcopter in 2015[13]. This paper addresses manned eVTOL, and the objective is to compare two main electrochemical power sources – lithium-ion batteries and hydrogen fuel cells, separately and in combination in a power-sharing mode – for an on-demand air taxi mission. The possible benefits of hybridization were first reported for a R-22 beta II helicopter[14,19], but it was a conceptual paper study. In this paper, we demonstrate power-sharing through hardware testing, develop refined steady-state and transient power models, calibrate them with test data, and carry out eVTOL sizing to investigate a baseline mission outlined by Uber[4], including a realistic assessment of the impact of technology growth. Preliminary results were presented by Ng and Datta[5] without demonstration of regulated power sharing. The final results are presented here including power sharing.

The first step is to develop new propulsion system models for the proper design and investigation of this new class of aircraft. There have been several efforts in recent years to build such models[14,15,16,17,18] and apply them to conceptual design of rotorcraft[19,20]. However, these models are all limited to steady-state, which make them adequate for sizing, but not for detailed design and performance analysis. Models that can predict both steady-state and transient behavior would allow for sizing as well as an analysis of a power plant for trim and transient maneuvers of an aircraft. Lithium-ion/polymer batteries and fuel cells are modeled as equivalent circuit networks (ECN) to capture the transient behavior using conventional resistor-capacitor (RC) models. Transient models predict voltage variation due to rapid changes in current. For batteries, they must also capture the variation due to state of charge.

The battery and fuel stack models are calibrated (for time constants) and validated (for phenomenological trends) using an in-house experimental set up. The set up consisted of a commercial fan-cooled proton exchange membrane (PEM) fuel stack, pressurized hydrogen equipment, and a lithium-polymer (Li-Po) battery connected in parallel to an electronic load as well as a flying quadrotor. A fuel cell requires many pieces of accessory equipment, called balance of plant, that incur power losses and add weight overhead. The setup was also used to determine these balance-of-plant losses and overheads.

The second step, sizing of e-VTOL, begins with state-of-the-art data for motor and battery weights as a basis for weight models. However, fuel cell weights cannot be readily inferred from data due to the wide variation in type of application and type of hydrogen storage. Top-level technology assessments can be found in the U.S. Department of Energy's continuing Hydrogen and Fuel Cell Program, automotive literature, and limited UAV applications reported in trade journals. These are not adequate for a proper weight estimation. Instead, a geometry and material based weight break-down is used, guided by (in-house) measurements from a commercial fan-cooled low-power stack, and reported literature on the custom-built liquid-cooled high-power automobile stacks of Honda[21] and Toyota[22,23].

Sizing of the aircraft calculates the minimum gross (total) take-off weight and payload weights that are achievable for a prescribed mission. These calculations are based on text book expressions, correction factors, and available data on existing aircraft, so that the primary focus remains on the impact of the new power plant. The results are compared for different power plant configurations: turboshaft, battery alone, fuel stack alone, and battery and fuel stack hybrid. They are also compared for edgewise and tilting prop rotor configurations.

Specific targets are based on Uber's white paper[4] for a demonstration of sizing. The maximum installed power was taken to be 500 kW (hover) with a cruise speed of 150 mph for 1 hr. Details of the mission are provided in the Aircraft Sizing section.

Finally, the effects of technology advances are investigated. The baseline results use parameters from flight-proven technology that has been successfully used in aircraft. These include battery specific energy, battery maximum current or C-rate (directly related to specific power), fuel stack specific power, and hydrogen tank weight fractions. Results are also calculated based on cutting-edge technology reported for each individual component; for example, a battery specific energy of 250 Wh/kg reported by the automobile industry, fuel stack specific power of 2 kW/kg reported by Toyota, and a hydrogen weight fraction of 7.5% – a target met by the Department of Defense hydrogen fuel cell program for pressured storage. These cutting-edge technology assessments provide insights for prioritizing technology investments. For example, the key barrier is the weight of the energy source and not the motors; including state-of-the-art fuel cells will provide for greater returns on payload than state-of-the-art batteries, at least for missions lasting more than 15 minutes; and in eVTOL, specific power (C-rating) might actually be the driving factor for battery weight, not specific energy.

The first part of the paper, Sections 2, 3, 4, and 5, deals with hardware and model development. The second part, Section 6 and 7, deals with weights and aircraft sizing. The second part relies on the weights and efficiencies measured in the first part. The first part draws its motivation from the results of the second part, which show that a battery-fuel cell combination can be superior to either power source alone. Thermal modeling is ignored in the first part. Cost and noise are ignored in the second part.

2. EXPERIMENTAL SETUP

A commercial 300 W PEM fuel stack and a 2800 mAh 3 cell lithium polymer battery were used to construct a simple test-bed to understand the system requirements and obtain test data for calibrating and validating the fuel cell and battery models. System requirements include balance of plant losses and overheads, which are later utilized for aircraft sizing. Due to the surrogate nature of the setup (non-flight worthy) these losses and overheads are expected to be conservative. Figure 1 provides a basic flow diagram of how power is delivered in a parallel hybrid system from the battery and fuel stack to a load. This applies to the setup used in power sharing demonstrations described in Section 5. The 'unregulated' version of power control architecture for this paper is a simple connection of the two power sources in parallel and adding diodes to ensure the current always flows away from the power source. The 'regulated' version adds controlled charging and discharging of the battery in a strategic manner to minimize the power plant weight. The data loggers record current and voltage over time.

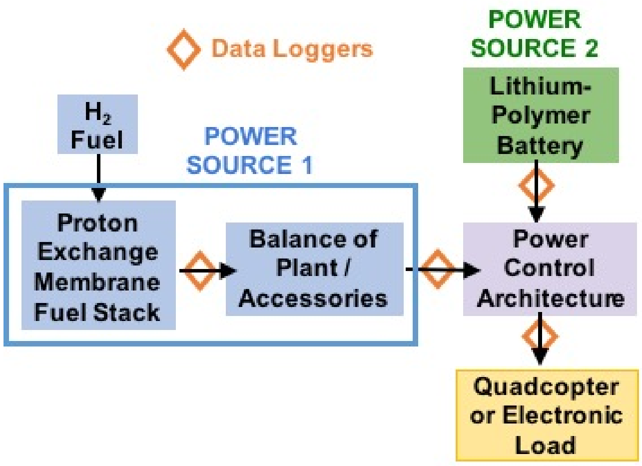

Figure 1: Flow diagram of a parallel hybrid power system.

The fuel stack controller controls the supply and purge valves to allow hydrogen flow in and out the fuel stack. This controller requires external power which can be provided by a power supply or a additional battery. The fuel stack operates around 50 V, so a DC-DC converter is used to reduce this voltage to that of the battery, to around 12 V. The power output from the fuel stack is connected in parallel with a battery. The combined power is then connected to a bench-top programmable electronic load for controlled tests. It is also connected to a quadcopter for tethered flight tests. A photograph of the hardware and detailed plumbing and wiring diagram are available in Ref.[5].

To calibrate the fuel stack and battery model, it was necessary to isolate the power sources and connect them individually to the load. These configurations are described in Section 3 in relation to the specific calibration processes.

The component weights are presented in Table 1. From these weights, the overhead mass associated with the DC-DC converter (including cables) was calculated to be 15% of the total mass. This represents the portion of the mass that would not be included in the specific energy of a fuel cell, and is later used in the Sizing section as a factor to obtain a more accurate system mass. The mass overhead for the hydrogen regulator is 13%, but this can likely be reduced for a digital pressure gauge and aerospace grade regulator. Data collection devices accounted for 4% mass overhead. Only the DC-DC step down mass overhead is used in the sizing calculations later. This low-end commercial fuel stack has a specific power of 0.1 kW/kg based on the fuel stack plus controller weight.

The primary losses occurred at the DC-DC converter, the diodes used to control power sharing, and the tether that delivered power to the load. Only the first is used in sizing later. The percent loss due to the DC-DC converter was found experimentally at a sweep of power levels using a bench-top electronic load in Ref.[5] and found to be an average of 25%. This steady-state characterization was compared to transient conditions during a quadcopter flight. Figure 2 compares the steady-state prediction (25% loss) to the measured power loss after the DC-DC step down, which was smaller during the actual flight (13% loss). This flight test value was used as the balance of plant power loss in the sizing calculations presented later.

Table 1: Mass breakdown of experimental setup

	Component	Mass (g)	% of Total Mass
Fuel Stack	Fuel Stack (300 W)		
	Supply Valve		
	Purge Valve		
	Cooling Fan		
	Total	2901	44.6
	FS Controller	433	6.7
	Display, FS	66	1
Balance of Plant/ Accessories	Battery for Controller	216	3.3
	DC-DC Converter	943	14.5
	Data Loggers (4)	158	2.4
	Displays, Data Logger (4)	54	0.8
	Cable Stub, DC Converter In	30	0.5
	Cable Stub, DC Converter Out	28	0.4
Hydrogen System	Hydrogen Regulator	840	12.9
	Hydrogen (35 L at 515 psig)	602	9.3
	Tube, Hydrogen Inlet	14	0.2
	Tube, Purge	3	0.05
Total		6503	

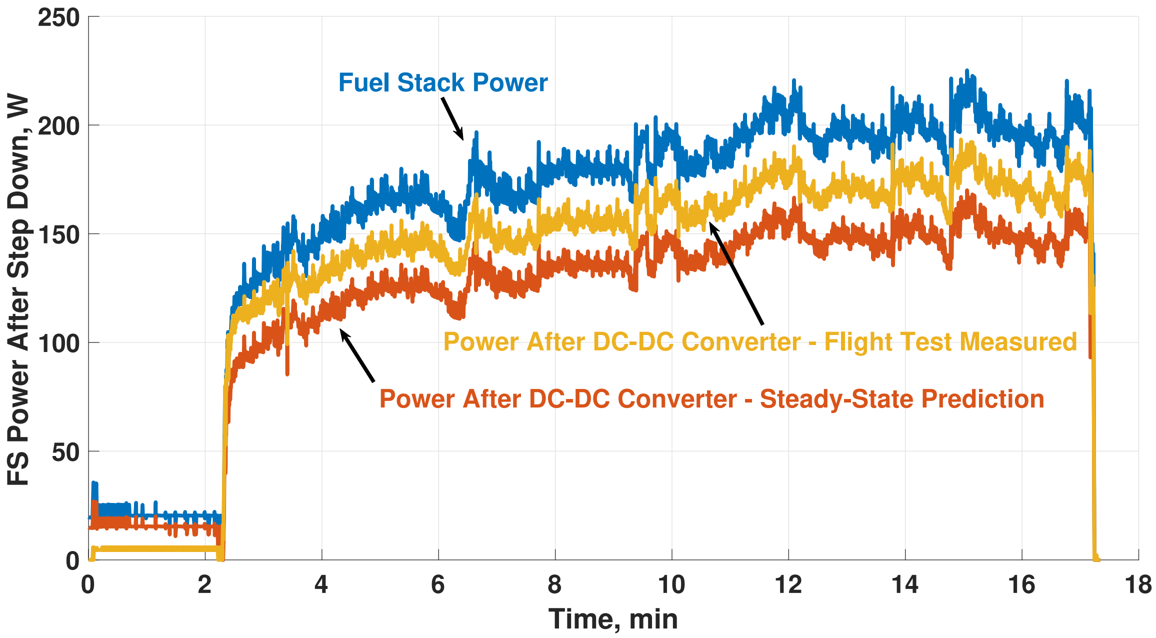

Figure 2: Power after DC-DC step down during quad-rotor hover – steady state prediction versus experiment.

3. MODEL DEVELOPMENT

3.1. Fuel Stack Steady-State Model

Power plant sizing calculations require steady state voltage versus current (i-v or polarization) curves. A steady-state model was developed based on a textbook description of the underlying electrochemical behavior of a fuel stack[25], extended to include empirical corrections for fuel stack temperature and humidity based on data from Ref.[26] and[27]. Then, transient operating characteristics were modeled using an equivalent circuit network (ECN). The ECN model captures the principal characteristics of transient dynamics[28,29,30,31] through a capacitative (first order) linear behavior. The circuit elements that determine the underlying time constants are calibrated using in-house experiments using the setup described earlier.

In Fig. 3, data from the fuel stack used in this paper are represented as FC-1 Data-1. The voltage is normalized by the number of cells in the stack and current is normalized by the total active area of the stack. FC-1 Data-2 is data from the same stack but from the manufacturer's specifications. They are close, as expected. Two other data sets are shown for comparison. FC-2 is from a state-of-the-art, aerospace grade, complete stack similar to that used by DLR. FC-3 is a single fuel cell tested by Yan[26] at 1 atm and 80°C. The power density in Fig. 3b is simply the product of cell voltage and current density shown in 3a.

The details of the model are described in Ref.[5]; the key results that enter sizing are summarized here. The calibrated constants are given in Table 2. The voltage $v(i)$ is a function the current density i and is equal to the ideal or open circuit voltage E_r minus activation, ohmic, and concentration losses. It consists of eight empirically derived thermodynamic constants: α_A, α_C, i_{0A}, i_{0C} (unitless constants), C (constant in volts), ASR_Ω (area specific resistance in Ωcm^2), i_L (limiting current in A/cm^2), and i_{leak} (leakage current in A/cm^2). The fitted models are shown as lines in Figs. 3a and 3b. The main difference is the high current and power from higher quality cells. Later in the sizing section, the polarization curve of FC-3 will be used, which is realistic but still conservative for an aerospace fuel stack.

At a given pressure (here, 1 atm) the steady-state characteristics depend mainly on the temperature and humidity of the anode and cathode. Cell-level data obtained from Ref.[26] were used to find the variation of the thermodynamic constants of the model with temperature and humidity. The results can be found in Ref.[5]. While these relations are available in the model, only one set of conditions were assumed for the Sizing section of this paper (T = 80°C, CRH = 100%, ARH = 100%).

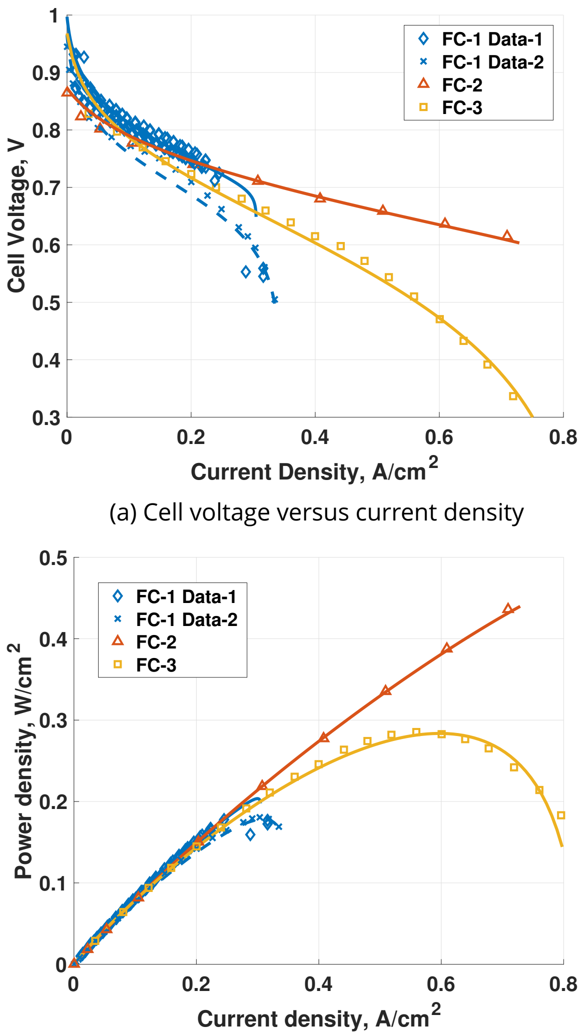

(a) Cell voltage versus current density

(b) Power density versus current density

Figure 3: Steady state characteristics of three different fuel cells; data and models.

Table 2: Thermodynamic constants for fuel cell steady state models

	FC-1 Data-1	FC-1 Data-2	FC-2	FC-3
α_A	1.1	1.1	1.1	1.1
α_C	0.18	0.15	0.17	0.15
i_{0A}	3 e-4	3 e-4	3 e-4	0.1
i_{0C} (A/cm^2)	1 e-4	1 e-4	1 e-4	1 e-4
i_L (A/cm^2)	0.31	0.35	0.8	0.85
i_{leak} (A/cm^2)	0.005	0.005	0.04	0.01
C (V)	0.01	0.06	0.005	0.15
ASR_{Ω} (Ωcm^2)	0.2	0.002	0.13	0.07

3.2. Fuel Stack Transients

To model the fuel stack's transient operating characteristics, an ECN for a single polarization model was used, shown in Fig. 4. E_r is the open circuit voltage. V and I are the voltage and current output by the fuel stack, respectively, where I is now a function of time. R_s is the electrolyte resistance (ohmic resistance in steady state) and R_{ct} is the charge transfer resistance causing a voltage drop across the electrode-electrolyte interface (activation and concentration losses in steady state). C_{dl} is the dielectric or double layer capacitance, which accounts for the transients and models the effects of charge buildup in the electrolyte at the anode-electrolyte or cathode-electrolyte junctions.

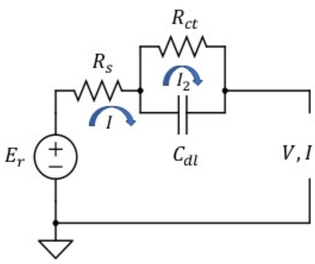

Figure 4: Basic equivalent circuit network of fuel stack.

The voltage V for current I is given by,

$$\begin{aligned} V &= E_r - R_s I - R_{ct} I_2 \\ &= E_r - (R_s + R_{ct}) I + R_{ct}(I - I_2) \\ &= v_{ss} + R_{ct}(I - I_2) \end{aligned} \tag{1}$$

(2)

where I_2 is found from the derivative of the voltage balance around the smaller loop,

$$R_{ct} C_{dl} \dot{I}_2 + I_2 = I \tag{3}$$

A more detailed derivation is available in Ref. [5].

Here, $v_{ss} = E_r - (R_s + R_{dl})I$ is the steady-state cell voltage corresponding to Fig. 3. This transient model collapses to the steady state model when the system is operating in steady state (when $\dot{I}_2 = 0$, $I_2 = I$, so $V = v_{ss}$). The values of the circuit components R_{ct} and C_{dl} were determined empirically. This was achieved by connecting the fuel stack output directly to an electronic programmable load. A step current was drawn from the fuel stack and the transient voltage response was recorded. A sample of this data along with the empirically calibrated constants for two different current levels are given in Fig. 5 and Table 3. As depicted in Fig. 5 , the magnitude of the transient is R_{ct} times the size of the current step ΔI, and the time for the voltage to achieve steady state is approximately 4τ, where $\tau = R_{ct} C_{dl}$ is the time constant. For the response to a step input, the model is given by the following equation, where t is the time after the step change in current occurs and ΔI is the magnitude of the step change.

$$V = E_r - \Delta I R_s - \Delta I R_{ct}\left(1 - e^{-t/(R_{ct} C_{dl})}\right) \tag{4}$$

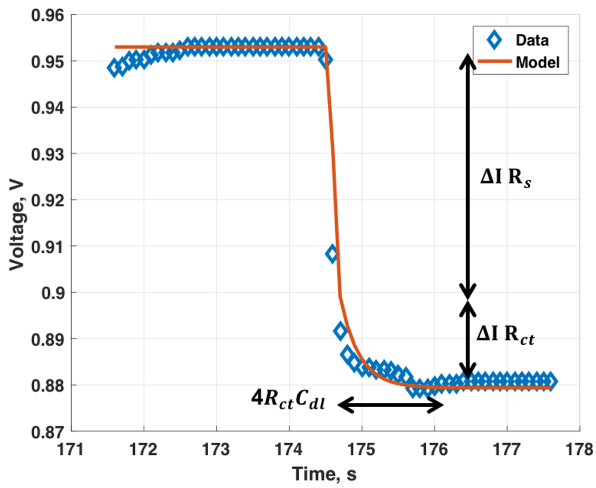

Figure 5: Voltage response to a step current drawn from a fuel stack.

The values of R_s, R_{ct}, and C_{dl} were found to depend on the magnitude of the current. They were calibrated separately for a very low current and a nominal current, as shown in Table 3. The resistor values are much lower at the nominal current, which indicates that the transients are of smaller magnitude and duration than at low current.

Table 3: Fuel stack ECN components calibrated for different current ranges

	Low Curr	Nominal Curr
Curr Density, A/cm^2	0.01-0.04	0.07-0.18
$\mathbf{R}_s$, $\Omega\ cm^2$	2.57	0.60
$\mathbf{R}_{ct}$, $\Omega\ cm^2$	1.22	0.09
$\mathbf{C}_{dl}$, F	0.23	0.26
Time Constant, s	0.28	0.023

3.3. Battery Steady State Model

In a battery, the open circuit voltage E_r is no longer constant (like it is in the fuel cell), but instead is a function of the battery's state of charge (SOC). The SOC describes the fraction of charge (in Ampere-hours, Ah) remaining in the battery over the total charge C (Ah) possible for supply. In its simplest form, it is given by Eq. 5, where I is the current drawn in Amperes, and t is the time in hours.

$$(5)\quad SOC = 1 - \frac{1}{C}\int I dt \qquad \text{for discharge}$$
$$= \frac{1}{C}\int I dt \qquad \text{for charge}$$

However, C itself can be a function of I, so this equation is hard to apply when the current changes with time. Typically, for Li-ion batteries, $C = C_{REF}/\alpha\beta$, where C_{REF} is capacity at a reference current I_{REF} and $\alpha(I)$ and $\beta(I)$ are rate factors associated with other currents and temperatures. Then, a more appropriate expression for SOC is,

$$(6)\quad SOC = 1 - \frac{1}{C_{REF}}\int \alpha\,\beta\,I\,dt \quad \text{for discharge}$$
$$= \frac{1}{C_{REF}}\int \alpha\,\beta\,I\,dt \qquad \text{for charge}$$

The rate factors α and β have to be determined empirically. The quantity Idt is the actual amount of charge supplied or delivered to the load; the quantity $\alpha\beta Idt$ is a notional amount of charge released or depleted from the battery with which the state of charge SOC is to be calculated.

A representative set of rate factors based on Ref.[32] are,

$$(7)\quad \alpha(I) = 1 + 0.4\left(\frac{I}{I_{REF}} - 1\right)\frac{I_{REF}}{C_{REF}}$$

$$(8)\quad \beta(T^\circ C) = 1 - 0.02093(T - T_{REF})$$
$$\text{where } T_{REF} = 23$$

Temperature also reduces the open circuit voltage (at all SOC).

$$(9)\quad \Delta E_r = 0.011364(T - T_{REF})$$

The variation in E_r with SOC means there is not a unique steady state I-V curve as with the fuel stack. As current is drawn, the SOC and E_r drop. This effect must be modeled. A fully empirical model based on the classical work of Shepherd[33] is adopted. For a constant current draw per unit area i, the Shepherd model has the following form.

$$(10)\quad v = E_r - IN$$

where

$$(11)\quad E_r = E_s - \frac{K}{SOC}I + A\exp\left[-B(1 - SOC)\right]$$

E_r is the open circuit voltage and v is the battery output voltage. E_s is a constant potential in volts, K is a polarization coefficient in Ω-area, N is the internal resistance times unit area in Ω-area, and A in volts and B (unitless) are empirical constants. SOC is the area specific state of charge. The original Shepherd model uses SOC from Eq. 5; if α and β are available, Eq. 6 should be used instead. In total, 4 empirical constants: E_s, K, A, and B describe the open circuit voltage E_r as a function of SOC, and the additional constant N is the resistance needed for closed circuit voltage v.

To calibrate the model for E_r, the battery was connected directly to a battery analyzer which discharged the battery at a very low constant i and measured v. The unit area was defined as the area of the cell, so the current density (current per unit area) is equivalent to the total current drawn from the battery. N was taken to be the summation of R_s and R_{ct}, the internal resistances of the battery, which were calibrated using the same method described in Section 3.2 for the fuel stack – by drawing a step current and recording the resulting voltage. The remaining values were calibrated empirically based on the discharge data.

The discharge data are shown in Fig. 6 and 7 for a 30 C, 2800 mAh, 3 cell lithium ion battery. Figure 6 uses a model based on the six empirical constants extracted from the 0.07 C discharge data, and shows how the model performs at different currents. Figure 7 uses empirical constants extracted from the 3.6 C discharge data. The main cause of this discrepancy at high currents is the change in K with current, obvious from Fig. 7, which shows how the model performs when the constants are extracted using data from 3.6 C. Here, the discrepancy is shifted to low currents. None of this is surprsing; even though the Shepherd constants have some basis in underlying phenomena, empirical models are always inadequate as prediction models; at best the constants can be evaluated for several current levels, as shown in Table 4.

The values for three different discharge currents are listed in Table 4. The resistance N was extracted from step input experimental data, and is equivalent to $R_s + R_{ct}$ of the battery from Table 5 presented later. The capacity C was extracted by fitting the constant current discharge data. This value is validated by comparing to the 'Discharge Capacity', which is calculated for each test by multiplying the current and the duration of discharge. It is slightly lower than the empirically fit capacity C, because the discharge was stopped when the battery voltage reached 9 V to avoid damaging the battery. Most of the constants vary with the operating current.

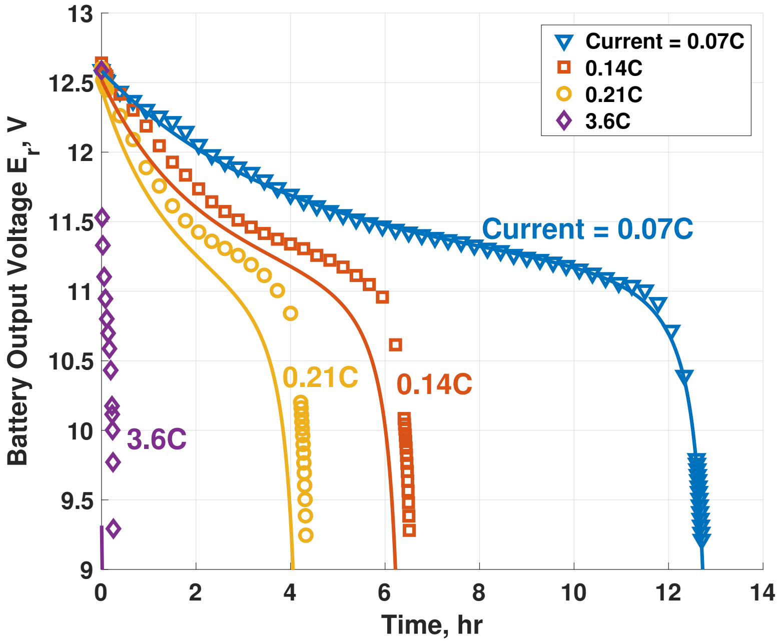

(a) Discharge model compared to experimental data.

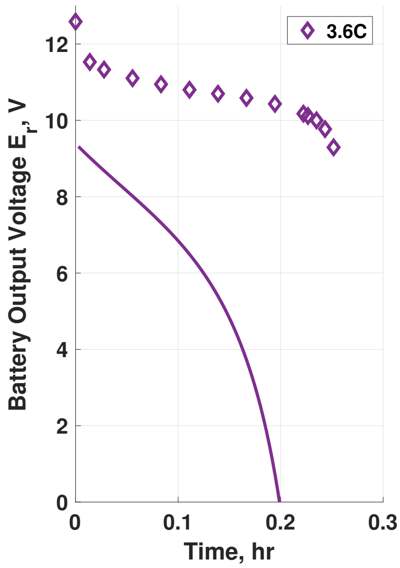

(b) Zoom in on small time range.

Figure 6: Shepherd model compared to test data; model parameters extracted at 0.07 C.

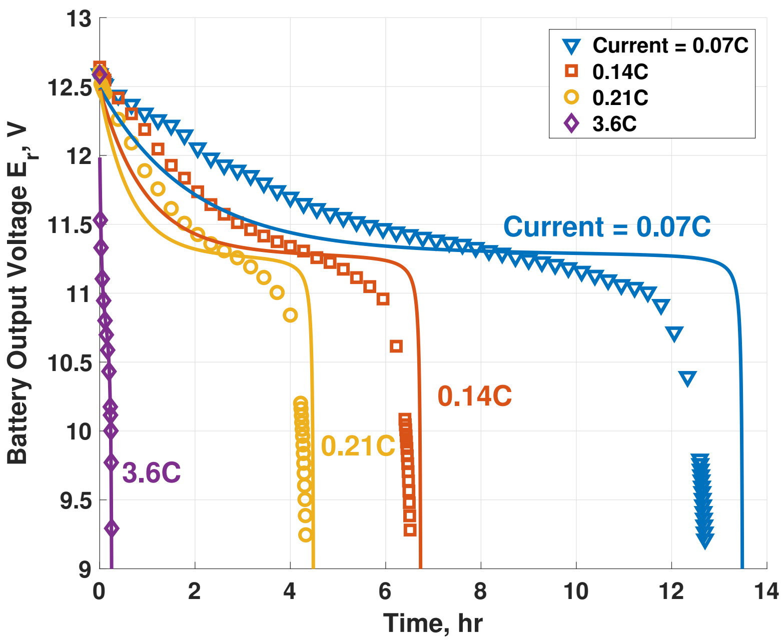

(a) Discharge model compared to experimental data.

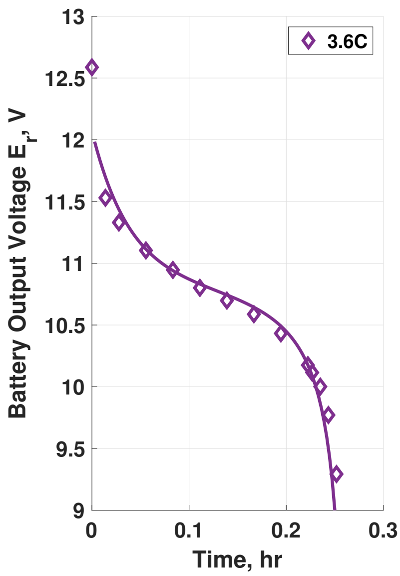

(b) Zoom in on small time range.

Figure 7: Shepherd model compared to test data; model parameters extracted at 3.6 C.

Table 4: Shepherd battery model constants for 2800 mAh, 30C, 3 cell lithium polymer battery

	Very Low Current	**Low Current**	**Nominal Operating Current**
Discharge Current, A	0.2	0.4-0.6	10
Discharge C-rate, h^{-1}	0.07	0.14	3.6
Discharge Capacity, Ah	2.54	2.61	2.54
E_s**, V**	11.3	11.3	11.3
K, Ω**-area**	0.25	0.1	0.015
Q**, Ah/area**	2.6	2.65	2.7
N, Ω**-area**	0.076	0.076	0.028
A**, V**	1.35	1.35	1.2
B	3.4	3.4	7.0

3.4. Battery Transient

The transient behavior of a battery can be modeled by an ideal ECN, like that of the fuel cell, for both are DC electrochemical sources. However, the open circuit voltage E_r is no longer constant, but instead a function of the battery's SOC. Many transient lithium ion battery ECN models have been developed in the past two decades for design of power systems in consumer electronics (see Ref.[32,34] for example) and hybrid-electric cars (see Ref.[24]). All of these models are semi-empirical and require extensive battery testing for temperature and frequency effects. The $E_r(SOC)$ would also have to be input separately as a function of temperature for all models.

The Shepherd model for $E_r(SOC)$ is retained to capture the nonlinear behavior of the steady-state and paired with an ECN model to capture the generally linear behavior of the transients. The transient model uses the same circuit diagram shown earlier in Fig. 4. The constants R_s, R_{ct}, and C_{dl} are extracted using the same method as the fuel stack. The results for low and nominal current ranges are presented in Table 5.

Table 5: Battery ECN components calibrated for different current ranges

	Low Curr	Nominal Curr
Current, A	0.01-2.4	9.3-13.5
C-rate, h^{-1}	0.0036-0.86	3.32-4.82
R$_s$, Ω	0.042	0.021
R$_{ct}$, Ω	0.034	0.007
C$_{dl}$, F	268.15	242
Time Const, s	9.12	1.69

While the capacitor values are larger than for the fuel stack, the resistor values are smaller. This manifests as voltage transients of a lower magnitude but longer settling time compared to the fuel stack. The time constant of the battery is approximately one order of magnitude larger than that of the fuel stack.

4. MODEL VERIFICATION

For lithium-ion batteries and PEM fuel stacks to be used in eVTOL, they must be able to respond to rapid transients caused by maneuvers or electrical faults. Experiments data were acquired to verify the models in the presence of these rapid transients.

Figure 8 shows fuel stack voltage with intentionally high amplitude and frequency transients. The results indicate that the model is generally capable of capturing the amplitude and waveform of the fuel stack's transient I-V characteristics. A small vertical shift is visible between model and experimental voltage, which can be attributed to measurement error or variations in temperature and humidity between the time of this test and the time of the steady-state model calibration (used to find v_{ss} in Eq. 1). The primary error in the model occurs at the beginning of the test, which appears as a longer transient behavior that occurs upon startup of the fuel stack, not captured by the present model.

The transient model is compared to the steady state in Fig. 8b. This steady state model is based on the FC-1 Data-1 model in Fig. 3a. This comparison reveals the first major conclusion: the transient model is almost identical to the steady state model. The steady state model is capable of capturing almost all of the behavior in the normal range of operating currents, so the transients in the fuel stack are not significant. This is a reflection of the fact that the values of R_{ct} and C_{dl} in Table 3 are fairly small for the normal operating current range. The error at the beginning of the test duration is perhaps due to a second, larger internal capacitance not captured by the ECN used in this model.

Similar data were collected for the lithium ion battery (Fig. 9). The model in this figure uses the empirical constants from the third set presented in Table 4. All three sets of constants were investigated and showed very small differences of less than 0.15 V. Comparison revealed the second key conclusion: unlike the fuel cell, here, the transient model is slightly different from the steady-state model, and in general provides an improved waveform. However, like in the fuel cell, there is again a vertical shift between the model and experimental voltage. The experimental voltage is lower, so it cannot be due to heating (rise in temperature increases voltage), but perhaps due to rate effects at higher currents (higher current reduces voltage), not included in the model ($\alpha = 1$ in the model). Additionally, discrepancies could be due to the battery's total capacity degrading over use; the constant voltage discharge data used to calibrate the model was collected after the transient experiment, and the battery's capacity had reduced from a nominal 2.8 Ah to a lower 2.6

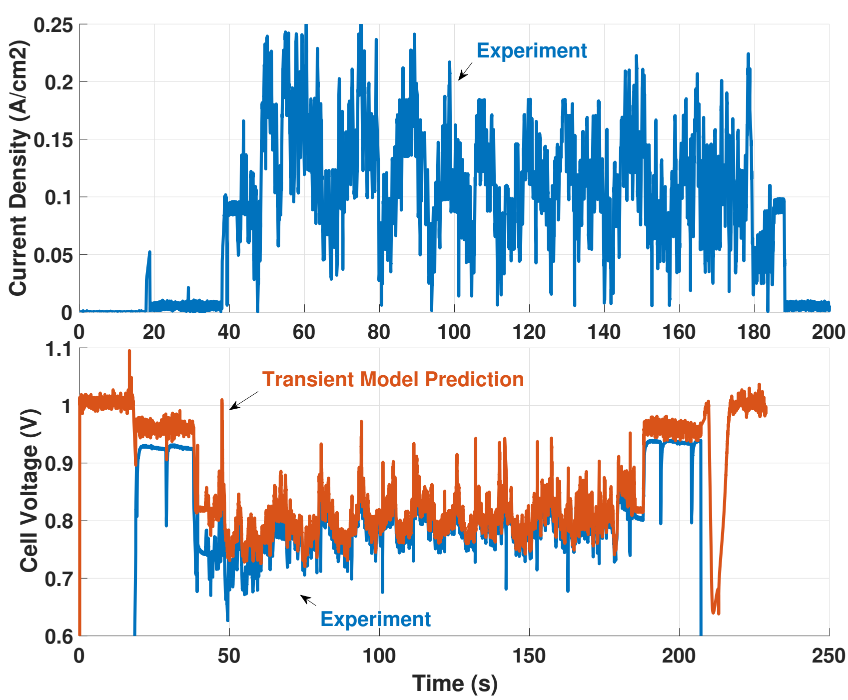

(a) Full test duration.

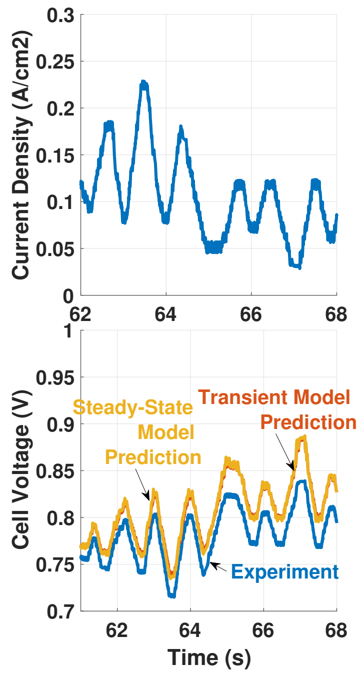

(b) Close-up comparing steady-state and transient models.

Figure 8: Model compared to experimental voltage for fuel stack for highly transient load.

Ah.

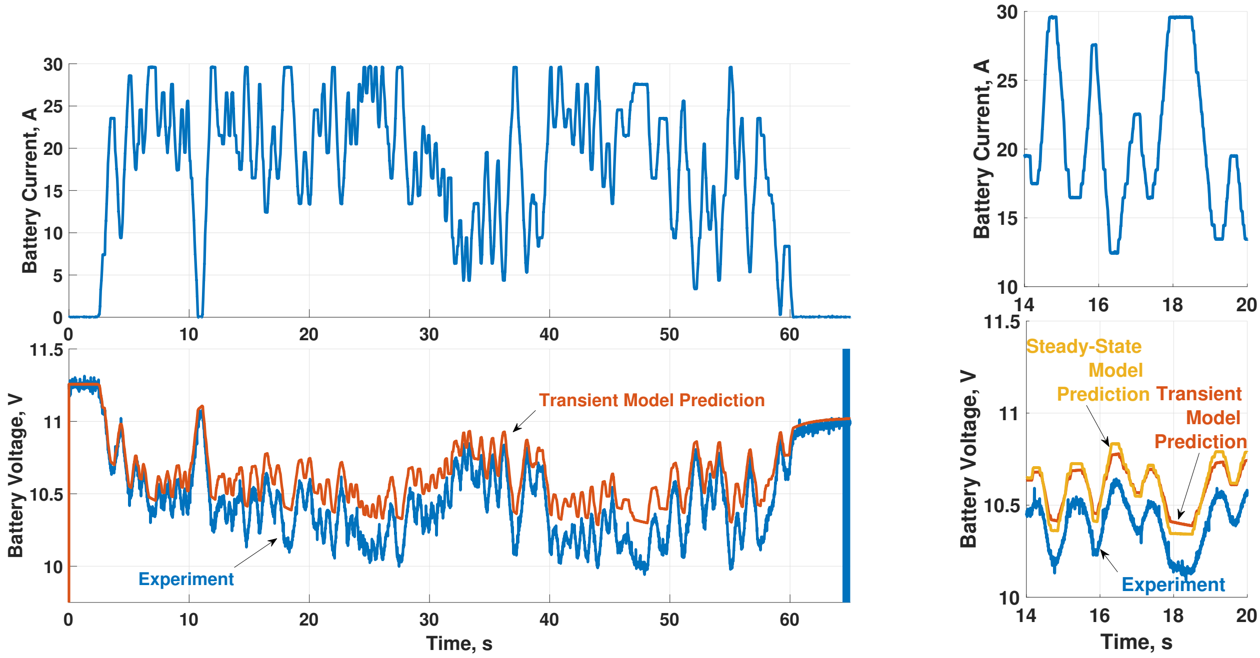

(a) Full test duration.

(b) Zoom in on small time range and comparing to steady-state model.

Figure 9: Model compared to experimental voltage for battery for highly transient load.

5. DEMONSTRATION OF POWER SHARING

5.1. Unregulated

The battery and fuel stack are connected in parallel and used to power a tethered quadcopter. The data from each power source and the quadcopter load are shown in Fig. 10. The flight test demonstrates the viability of using the two power sources in a hybrid power plant. The architecture for the unregulated system is trivial; the two components are connected in parallel with only a diode in series with the fuel stack and a DC-to-DC converter, the same arrangement shown earlier in Fig. 1. The power flow is not regulated at all; the two components are left to operate based solely on their i-v characteristics. The key conclusion from Fig. 10 is that they form a natural combination working in tandem – the battery voltage drops with depleting SOC, diminishing its share of power. This causes the fuel cell voltage to also drop, increasing its share of power (Fig. 3). Thus, the total power supply is maintained. Regulation would be required to force them to not work in tandem, and instead share the supply of power as desired. This is an essential requirement for eVTOL, where the fuel stack is sized to low power cruise mode and the battery supplements during high power segments of the mission to minimize power plant weight.

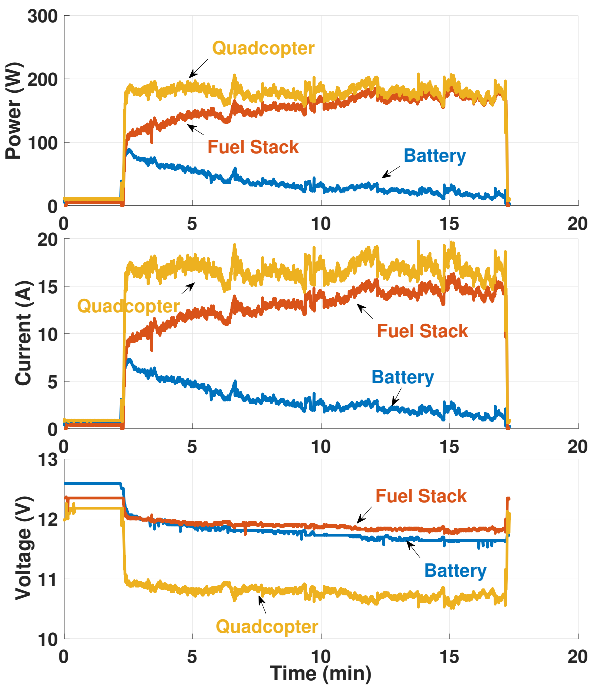

Figure 10: Experimental power, current, and voltage of battery, fuel stack, and quadcopter during hover.

5.2. Regulated

A regulated system would conserve battery energy and use hydrogen energy whenever possible, because hydrogen energy is more weight-efficient. The battery would only be used during high power portions of the mission to supplement the fuel stack. Additionally, if the battery is depleted, the excess power from the fuel stack can be used to recharge the battery. This is illustrated in Fig. 11.

In the regulated case, the battery no longer discharges during the low-power phases: spin-up, transition, cruise, and spin-down. Thus, less energy is drawn from the battery and more from the fuel stack. The regulated power sharing strategy reduces the total weight of the power plant compared to the unregulated strategy because batteries suffer from low specific energy but higher specific power.

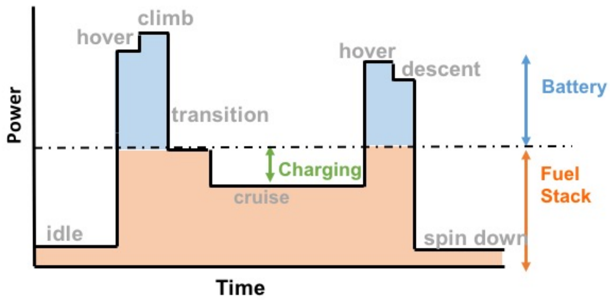

Figure 11: Power supplied by fuel stack and battery in regulated operation for a notional mission power profile.

To implement the regulated power sharing architecture, a circuit was constructed based on a modification to a circuit in Ref.[10]. It is shown in Fig. 12. The fuel stack and battery are still connected in parallel with a diode to prevent current flow into the fuel stack. The additions to the unregulated circuit are the DC-DC step up and the two switches to control charging or discharging of the battery and the DC-DC step up. The switches are voltage controlled solid state relays activated by an Arduino. When the relay on the left is closed, the diode in that branch limits the current flow so that the battery can only discharge. When the relay on the right is closed instead, the diode in that branch channels the current flow in the direction to charge the battery. The step up increases the voltage to charge the battery, which allows for faster charging.

The Arduino sets the switches open or closed depending on the battery voltage and load power. The various operating states are described in Table 6.

- State 1: The battery is fully charged and the load power is low. All the power is supplied by

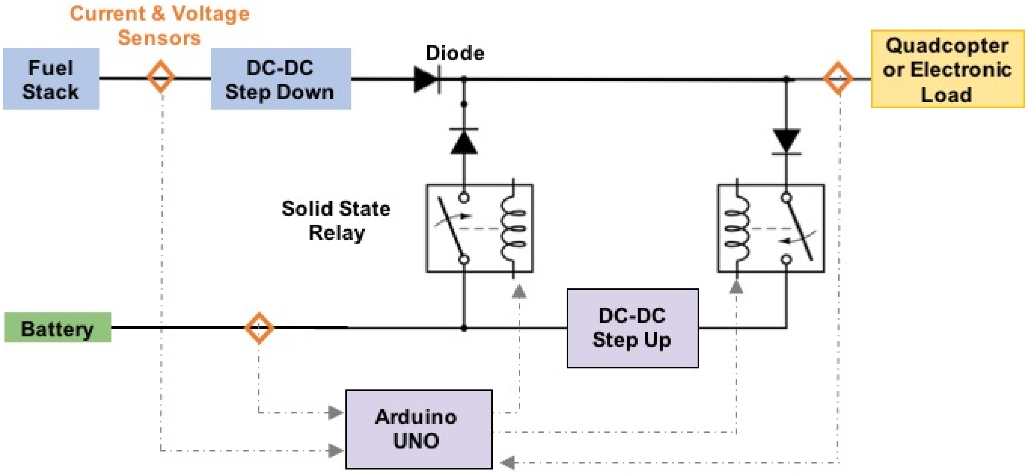

Figure 12: Circuit diagram for regulated power sharing operation.

the fuel stack, and the battery is completely disconnected from the circuit. Charging is not allowed to avoid overcharging the battery.

- State 2: The battery is fully charged and the load power is above that which can be supplied by the fuel stack alone. The battery discharge switch is closed, allowing the battery to share the load with the fuel stack.
- State 3: The battery is partially depleted but still above its safe minimum voltage. The load power is low. The battery is prevented from discharging because the fuel stack is capable of providing all the necessary power.
- State 4: The battery is in the same range as 3, but the load power is above that which can be supplied by the fuel stack alone. The battery discharge switch is closed, allowing the battery to share the load with the fuel stack.
- State 5: The battery is completely depleted to its minimum safe voltage. The load power is low. The battery discharge switch is open so it cannot provide power to the load. The fuel stack provides all the power to the load and also charges the battery if excess power is available.
- State 6: The battery is completely depleted but the load power is above the maximum fuel stack power. However, to prevent damaging the battery, it is still not allowed to discharge. If this case is ever reached, the battery was not sized adequately for the mission.
- State 7: If the battery charge or discharge current exceeds the maximum rated current, the switches open to disconnect it from the circuit as a safety precaution.

The first six states are demonstrated experimentally in Fig. 13. For this demonstration, the cutoff for 'high' or 'low' load was 20 W. This is an arbitrary number chosen for illustration purposes. The cutoff for 'high' battery voltage was 12.3 V and the cutoff for 'low' battery voltage was 11.3 V. The blue 'Dchg' and red 'Chg' lines indicate the time segments where the battery is discharging and charging, respectively.

When the fuel stack and battery are power sharing (cases 3 and 5), the sum of the fuel stack and battery currents equal the current received at the load ($I_{fs} + I_{bat} = I_{load}$). The sum of the fuel stack and battery power is slightly greater than the power received by the load ($P_{fs} + P_{bat} > P_{load}$), due to losses across the diodes and wires. The same is true for the other cases – current in conserved and accurately illustrates the 'power sharing', while power is not conserved due to losses in the circuit.

The circuit used in this demonstration is the one shown in Fig 12, with the exception of the DC-DC step up, which is an optional additional refinement to be incorporated in future work. Without the DC-DC step up, the voltage to charge the battery is lower, and thus charging occurs more slowly, which is undesirable. However, even without the step up, the total battery mass (driven by total required battery energy) for the notional mission is smaller in the regulated circuit compared to the unregulated circuit.

Table 6: Operating states of power sharing control circuit.

State	Battery Voltage	Load Current	Switch States		Power Source
			Discharge	Charge	
1	High	Low	0	0	Fuel Cell
2		High	1	0	Fuel Cell + Battery
3	Medium	Low	0	1	Fuel Cell + Charge Battery
4		High	1	0	Fuel Cell + Battery
5	Low	Low	0	1	Fuel Cell + Charge Battery
6		High	0	0	Fuel Cell
7	Battery Current High (Safety Disconnect)		0	0	Fuel Cell

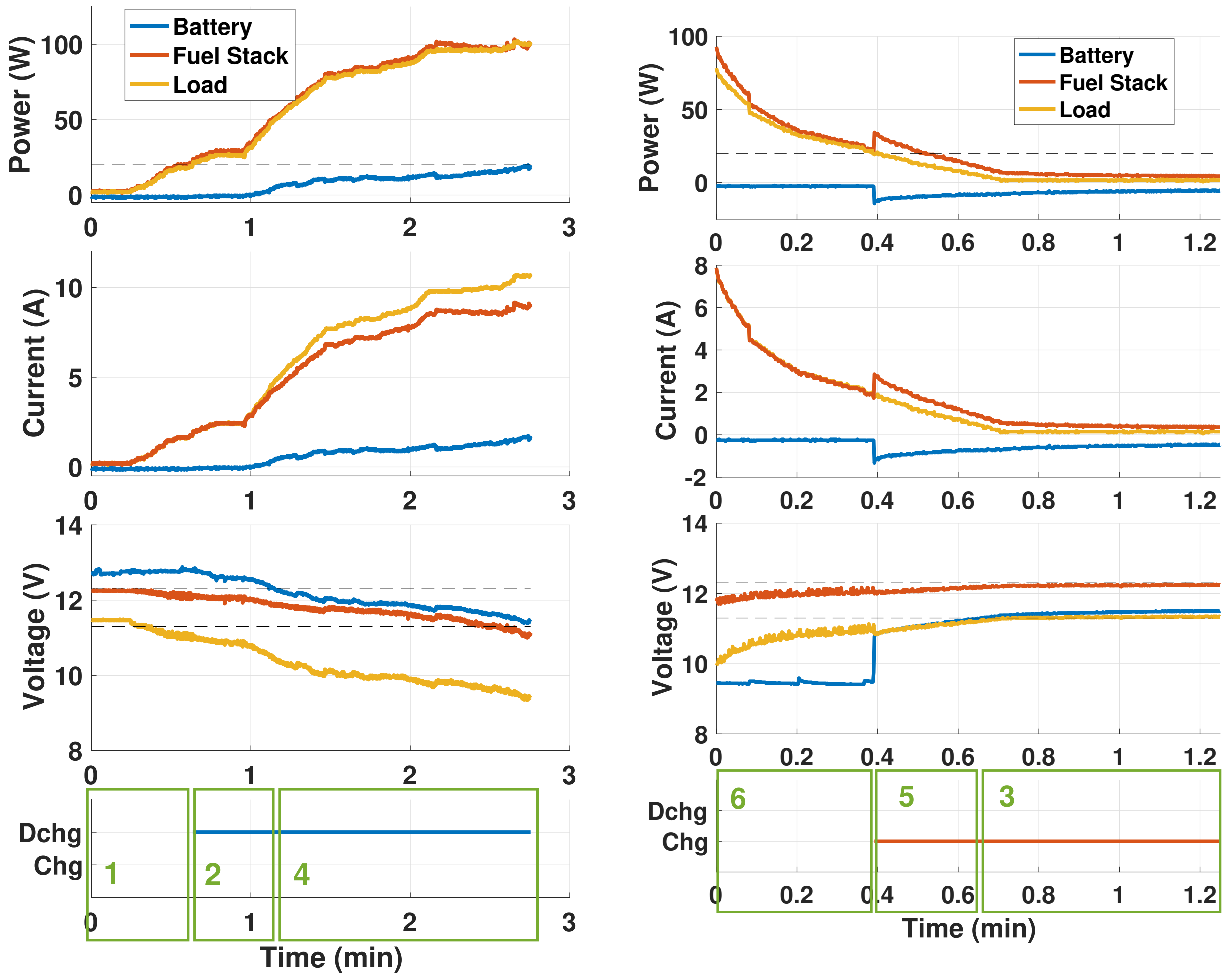

Figure 13: Demonstration of power sharing circuit's six operating modes. Critical load cutoff marked at 20 W, critical high and low voltage cutoffs marked at 12.3 and 11.3 V respectively. Blue 'Dchg' and red 'Chg' lines indicate battery discharging and charging, respectively. Green boxes indicate the state demonstrated at each segment of time.

6. POWER PLANT WEIGHT

This section describes models to calculate fuel cell and battery system weights required for aircraft sizing. These weights depend on the operating characteristics (models of which were described earlier) desired from the power plant. Also described are motor weights.

6.1. Motors

Several manufacturers have introduced AC permanent magnet synchronous motors for powering aircraft in the past few years. Figure 14 shows weights of 23 motors from six manufacturers (Thin Gap, Joby, EMRAX, YASA, Siemens and UQM), plotted versus maximum continuous torque and power. Of these, 17 motors are designed for aeronautical applications. The motors range from $4 - 260$ kW continuous power, $3-1000$ Nm continuous torque, and $1.3 - 95$ kg weight. The inverter/controller weight lies between $16-28$ kg for the heavier UQM motors. The operating voltage is typically between $250-425$ volt DC.

Several weight trends can be found in recent literature[14,15,35]. Here, only the 17 aeronautical motors are used. Figure 14 shows how the weights of these motors scale with maximum continuous torque. They follow the relation,

$$
\begin{aligned}
&\ln W_{kg} = -0.91 + 0.71 \ln Q_{Nm} \\
(12)\quad &W_{kg} = 0.4025\, Q_{Nm}^{0.71} \qquad \text{with} \pm 30\% \text{ error} \\
&\ln W_{kg} = -0.89 + 0.89 \ln P_{kW}
\end{aligned}
$$

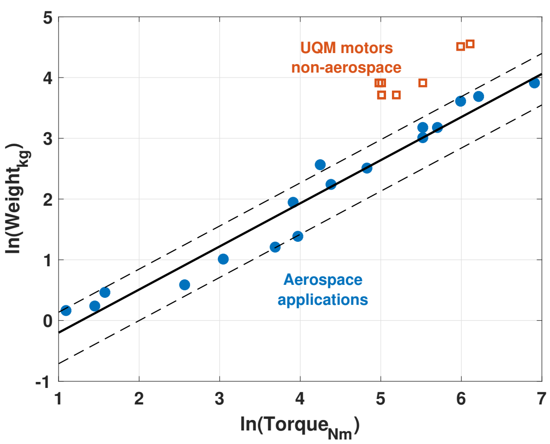

Figure 14: **Motor weight versus continuous torque with ± 30% error bands; log scale.**

6.2. Lithium Ion Batteries

The Li ion battery model assumes n_s units in series arranged in n_p cells in parallel. The total number of cells is $n_p \times n_s$. A schematic is given in Fig. 19. The series-parallel arrangement allows for adding energy while keeping a fixed voltage output. The cells are assumed to be identical. The battery voltage is $V_B = n_s\, v_c$. The current through each cell is i_c. The currents add, so the battery current $I_B = n_p\, i_c$, or equivalently the battery capacity C_B (Ampere-hour, Ah) is related to the cell capacity C_c as $C_B = n_p\, C_c$. The energy capacity E_B (Watt-hour, Wh) is then $E_B = C_B\, V_B = n_p n_s\, C_c\, v_c = n_p n_s E_c$ which is the total number of cells in the battery times the energy capacity of each cell. The battery weight is calculated from the weight of each cell.

For a known output voltage V_B, mission energy E_B, and a choice of cell C_c, the minimum weight is calculated as follows. The main equation is the cell weight versus capacity based on statistical fit of current generation Li ion cells. The data in Fig. 15 are from twelve manufacturers; however, the equation uses data from only eight that are specifically designed for electric cars (shown as filled symbols in Fig. 15): AESC (NISSAN Leaf), LG Chem (Renault), Li-Tec (Daimler), Li Energy (Mitsubishi), Toshiba (Honda) and Panasonic (Tesla Model S).

$$
\begin{aligned}
& n_s = {}^{V_B}\!/_{v_c} && (v_c = 3.7 \text{ volt for Li ion}) \\
& C_B = {}^{P_B}\!/_{V_B\,\zeta} \quad \text{or} \quad E_B/v_B, && \\
& && \text{(whichever is greater)} \\
(13)\quad & n_p = {}^{Ah_B}\!/_{Ah_c} && \\
& w_c = (0.0075 + 0.024\, Ah_c)\, f_T && \text{(kg)} \\
& W_B = w_c\, n_p\, n_s && \text{(kg)}
\end{aligned}
$$

The inputs are voltage output V_B (volt), maximum power P_B (Watt), and the C rating ζ (hr^{-1}). P_B/V_B is the current draw I_B. The minimum battery weight is found when I_B is the maximum (continuous, for the duration of P_B) discharge current. Then, $I_B = \zeta C_B$. If the C-rate ζ is known, the required charge capacity C_B can be found.

Consider a segment of a mission where power P_B (W) is required over time Δt. If the voltage is V_B (V), then the charge capacity needed will be $\Delta C_B = P_B \Delta t / V_B$. However, if the C-rate is ζ, the power delivered can at most be $\zeta \Delta C_B V_B$. To ensure this equals P_B, the charge capacity must at least be $\Delta C_B = P_B / \zeta V_B$. Thus,

$$
(14)\quad \Delta C_B = \max\left(\frac{P_B \Delta t}{V_B},\ \frac{P_B}{\zeta V_B}\right)
$$

where the first quantity is the capacity required to delivery the energy required, and the second is the

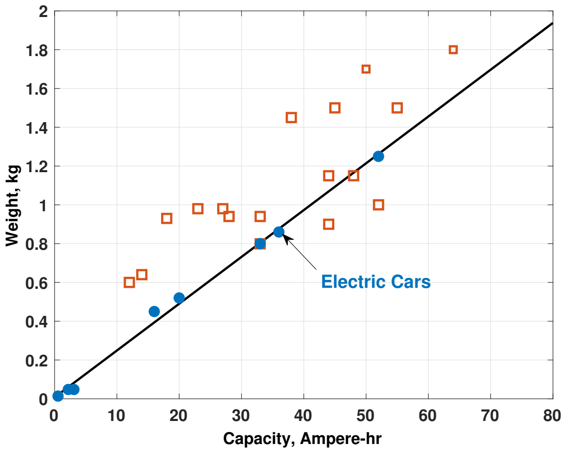

Figure 15: **Lithium ion cell weights versus capacity in Ampere-hr.**

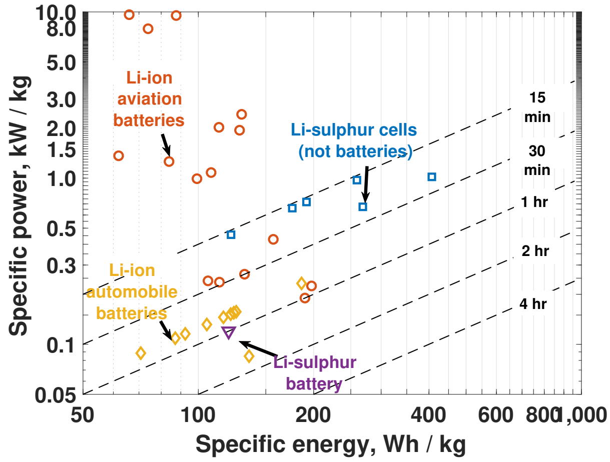

Figure 16: **Li ion and Li S cell specific power and energy (up to 80% discharge).**

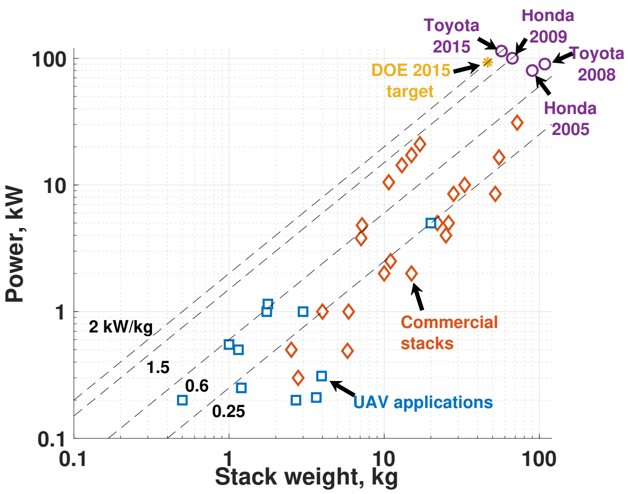

Figure 17: **PEM stacks of power 0-100 kW.**

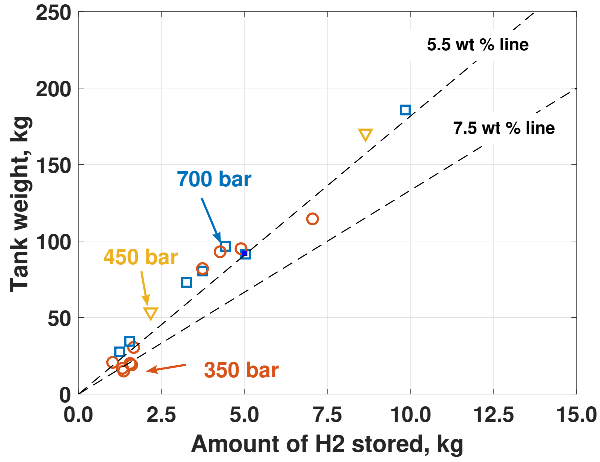

Figure 18: **Gaseous (300, 450 and 700 bar) and liquid hydrogen storage.**

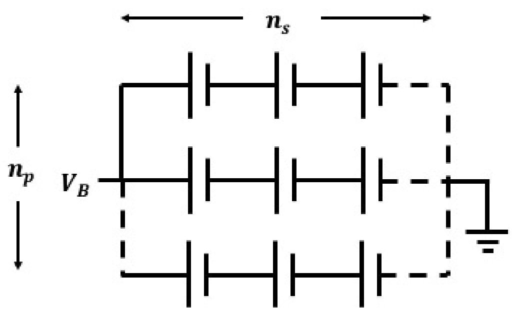

Figure 19: Schematic of batteries connected in series and parallel.

capacity required to deliver the power required. If the second is greater, it means more energy is necessary for the mission than is being carried just to satisfy the power demand.

The optimal condition is when both are the same.

(15) $\zeta = 1/\Delta t$

For example, if high power is required only for 5 min (e.g. for hover), then $\zeta = 5/60$ hr^{-1}. If a battery of this C-rate is not available, then more capacity must be carried on board than what is needed to deliver the energy. Typically, Li-ion chemistries that store high energy have low C-rates and vice-versa (2-4 C for 80-100 Wh/kg; 0-1 C 150-200 Wh/kg), thus the total capacity must be evaluated carefully based on power segments and available C-rates.

In general, for constant power, P_B/ζ gives the energy in Watt-hr. For varying power, the energy is input from the mission, and the ζ found from the maximum power required. n_s and n_p are rounded to higher integers. The factor f_T is a technology factor; $f_T = 1$ places the specific energy at 150

Wh/kg for $\zeta = 1$ which represents a nominal state of the art at the battery level. The state of the art in cell level energy and power of these Li ion batteries are shown in Fig. 16. The cells used for the weight equation can be found along the 1 hour endurance line (except for the NISSAN Leaf which falls near the 2 hour endurance line). The energy is obtained assuming up to 80% discharge and the power is based on the maximum continuous C-rating. Some of these cells are designed for higher power (greater maximum continuous current, i.e. C-rating) and some for higher energy, but it is apparent that in general they are energy limited, and only able to provide high specific power for short duration (less than 15 minutes).

6.3. PEM Fuel Stack

Proton Exchange (or Electrolyte) Membrane (PEM) fuel cells have lower specific power compared to batteries (due to a heavy balance of plant) but can provide dramatic increase in energy stored due to its hydrogen fuel. The degradation of its performance with low pressure is a problem in aeronautics, but not for on-demand air-taxi eVTOL, where the flight altitudes are expected be remain low. The problem of hydrogen storage and boil-off is also less significant in aviation compared to cars, and lesser even for on-demand air-taxi eVTOL, because of the shorter duration missions and only a few hours of hydrogen storage compared to weeks. Thus the significant progress made in the past decade toward lighter gaseous hydrogen storage can be exploited to full advantage.

A PEM fuel cell system consists of the stack and the hydrogen tank. For the stack, statistical weight models are difficult (see Fig. 17 for stacks of $0.4 - 100$ kW of continuous net power), because of drastic variations based on cost (cell materials/catalyst), duty cycles (construction), and applications (household to cars to aircraft APU to UAVs). Specific powers can easily range from 0.1 kW/kg for inexpensive laboratory grade stacks to 2.0 kW/kg for expensive automobile stacks.

A model suitable for design is one that is connected to stack geometry, materials, and operating characteristics so that improvements in constituent parts can flow into sizing. A simple model can be constructed as follows. Cells, shown in a schematic in Fig. 19, are assumed to be in series within a stack (which they typically are). Each cell is essentially a membrane electrode assembly (MEA). If the cross sectional area is k_A times the active area A_c, the area density of each MEA ρ_c (kg/m^2), thickness t_c (m), n_p cells in a stack, and an overhead fraction of η_O (to account for gaskets, seals, connectors and end plates), then the weight W_{FS} and volume L_{FS} become

$$W_{FS} = \eta_{OW}\, W_{FS} + n_p\, k_A\, A_c\, \rho_c$$

$$L_{FS} = \eta_{OL}\, L_{FS} + n_p\, k_A\, A_c\, t_c$$

The maximum power output P_{max} is related to the maximum cell power density p_{cmax} by $P_{max} = p_{cmax}\, n_p\, A_c$. Then the weight model is

$$(16) \quad W_{FS} = \frac{k_A}{1 - \eta_{OW}}\, \rho_c\, \frac{P_{max}(1 + f_{BOP})}{p_{cmax}}$$

A value of $k_A = 4$ (conservative) is assumed in this paper. Published data from Honda[21] and Toyota[23,22] suggest $\rho_c = 1.57$ kg/m^2, $t_c = 0.001301$ m and $\eta_{OW} = 0.3$. The number of cells and active area are found from output voltage and power as: $n_p = V/v_c$ and $A_c = P/(n_p\, p_c)$. The design cell voltage υ_c (for maximum continuous power) is selected either to minimize the combined stack and tank weight or to ensure enough power margin (adequate maximum rated power). The factor f_{BOP} is the 20% balance of plant power for the fuel stack used in this paper.

The fuel flow rate, at any given power, is related to the cell voltage. Corresponding to p_{cmax}, a v_{cmax} can be found from the cell $i - v$ characteristics. In general, at any power P, cell power density is $p = P/n_p\, A_c$ and given p, the corresponding v can be found. The fuel flow rate is

$$(17) \quad \dot{W}_F = \lambda_H\, \frac{m_H}{N\, F}\, \frac{P(1 + f_{BOP})}{v}$$

and tank weight

$$(18) \quad \dot{W}_{H2T} = \frac{1}{\eta_{BO}\;\; w_{\%}} \int \dot{W}_F\, dt$$

where λ_H is the effective stoichiometry (1 for no loss in hydrogen utilization), m_H is the molar mass (2.016×10^{-3} kg/mole), $N = 2$, $F = 96485$ Coulomb/mole, P is the stack output power in Watt, v the operating cell voltage in volts, and η_{BO} is the boil-off efficiency factor. The effective stoichiometry $\lambda_H = S_H\, \eta_H$, where S_H is the chemical stoichiometry (number of hydrogen molecules participating in reaction $= 1$) and η_H is the hydrogen utilization factor (typically $1 - 1.02$). The tank weight W_{H2T} is found from fuel weight W_F divided by the tank weight fraction $w\%$. For compressed hydrogen at 350 or 700 bar, the state of the art for long duration storage is 5.5% ($w_{\%} = 0.055$) (see Fig. 18). Tolerating some hydrogen boil-off should allow greater weight fractions of 7.5% – 15%, or perhaps even 30%. The tank model is simply this weight fraction.

7. EVTOL SIZING

Sizing involves calculating the minimum gross (total) take-off weight (W_{GTO}, lb) and engine power (P_H, hp) needed to carry a prescribed payload (W_{PAY}, lb) over a prescribed mission. The major dimensions of the configuration — rotor(s) radius and solidity and wing(s) span and chord — fall out of sizing. If the maximum power is prescribed as an input, sizing involves calculating the maximum gross take-off weight and payload. If power and gross take-off weight are both prescribed (as in the Uber paper[4]), then the aircraft is already sized, and the task is only to find the payload.

We begin with the last assumption, that is, both maximum power and gross weight are prescribed (following the Uber paper), then proceed to sizing with only the maximum power prescribed. An elementary mission is considered, representative of a simple on-demand intra-city air-taxi operation: only 5 minutes of hover and 1 hour of cruise.

7.1. Power and Gross Weight Prescribed (Uber Elevate)

The Uber Elevate paper gives a maximum hover power P_H of 500 kW (670 hp) and gross take-off weight W_{GTO} of 1800 kg (4000 lb) (see Table 7 for other requirements). The power loading W_{GTO}/P_H (6 lb/hp) is compared with existing VTOL aircraft in Fig. 20. The power loading varies with disk loading ($DL = W_{GTO}/A$, where A is the total disk projected area of all lifting rotors) as per the text book expression:

$$(19)\quad P_H = \frac{1}{FM}\, W_{GTO} \sqrt{\frac{DL}{2\,\rho}}$$

where ρ is the air density and FM the Figure of Merit (ideal induced power in hover divided by actual power). With an efficient rotor (high Figure of Merit, between $\approx 0.6-0.8$), the disk loading will fall in the range of $15-20$ lb/ft^2 — closer to tiltrotor values than edgewise rotor helicopters. High disk loading implies smaller rotor(s), therefore less drag in cruise, resulting in high aircraft lift to drag ratio (L/D) (Fig. 21).

The power to cruise at speed V_C is:

$$(20)\quad P_C = \frac{W\,V_C}{L/D}$$

With $W = W_{GTO}$, and cruise power and speeds from Table 7, the L/D values obtained are clearly far beyond what are achieved by current VTOL aircraft (Fig. 21) (and closer to commercial jetliners). The sizing results will later show that this assumption is unnecessary; even with realistic L/D with modest (10-20%) improvements, missions like the one above can be flown with eVTOL. Figure 22 shows data from XV-15 tests[36]. The aircraft L/D changes as the nacelle tilts and wing flaps deploy to trim and fly at different speeds. The lines represent polynomial fits used later in sizing calculations. The dashed lines indicate 10 and 20% technology improvements.

Table 7: **Mission requirements for a representative on-demand electric-VTOL aircraft from Uber Elevate[4]**

Requirement	Target	
Hover/take-off pwr	500 kW (670 hp)	MRP
Max cruise pwr	120 kW (161 hp) - at 200 mph	IRP
Max endurance pwr	70 kW (94 hp) - at 150 mph	MCP
Range, intra-city	80 km (50 miles)	
Range, inter-city	240 km (150 miles)	
Gross weight	1800 kg (4000 lb)	
Payload	2-4 people	400 lb

IRP=Intermediate Rated Power, MRP=Maximum Rated Power, MCP=Maximum Continuous Power.

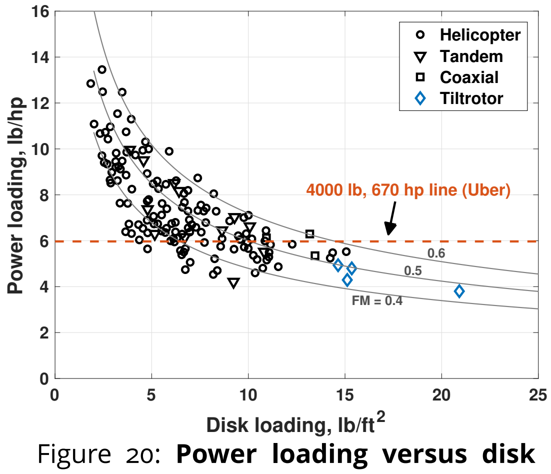

Figure 20: **Power loading versus disk loading of VTOL aircraft; FM lines assume sea-level density on a standard day.**

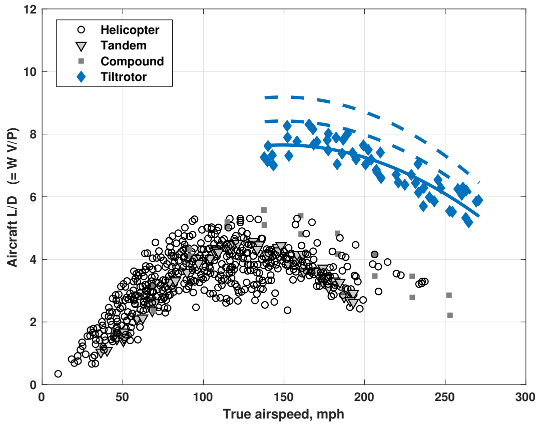

Figure 21: **Aircraft L/D versus true air speed of VTOL aircraft; the dashed lines are 10% and 20% improved L/D from tiltrotor aircraft; stars are based on target power, speed, and weight from**[4]

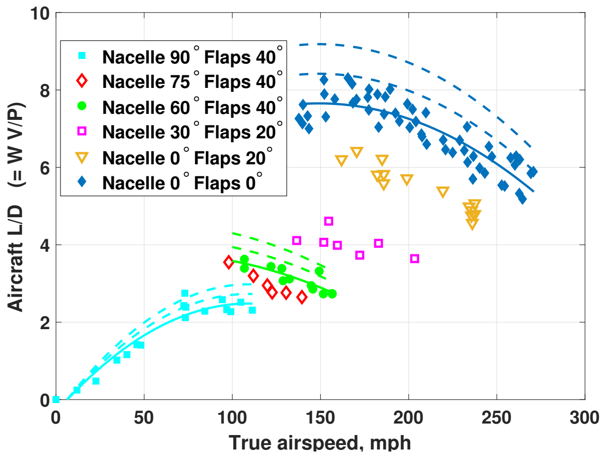

Figure 22: Aircraft L/D versus true air speed of XV-15 tiltrotor; the dashed lines are 10% and 20% improved L/D.

7.2. Sizing for Prescribed Power

The maximum power is prescribed as an input. Sizing calculates the maximum gross take-off weight W_{GTO} and payload W_{PAY} for a range of disk loading DL.

The gross take-off weight is the sum of empty weight and the useful weight. The empty weight W_E is the structural weight, the power-plant weight, and a generic group of all other weights (typically 30% of empty weight; $f_{WO} = W_{Oth}/W_E = 0.3$). This group of all other weights includes the operating weight (fixed useful load plus weight for equipment and systems), vibration damper weight, and any contingency weights. The useful weight is the payload weight (the purpose of flight) and supporting weight (mainly fuel and crew, weight to carry out the purpose). We consider only fuel in this category, the crew is included in payload. These break-downs are shown below.

$$\begin{aligned} W_{GTO} &= W_E + W_{USE} \\ W_E &= W_S + W_P + W_{Oth} \\ W_{USE} &= W_{PAY} + W_{FUEL} \end{aligned} \tag{21}$$

For each disk loading, the steps are:

1. From the maximum engine power, calculate the maximum W_{GTO}. Typically $P_{MAX} = PF\ P_H$, where PF is an installed power factor for excess power and P_H is from Eq. 19. Here, assume $PF = 1$ for minimal hover capability. Consider $FM = 0.6$ to begin with.

2. From disk loading and number of rotors, find radius R. With R known, FM can be updated. Simple momentum theory results are used. The following are assumed: solidity $\sigma = 0.1$, airfoil lift coefficient $c_l = 5.73\,\alpha$, drag coefficient $c_d = 0.01 + 0.2\,\alpha^2$, α is the mean sectional angle of attack, tip Mach number $M_T = 0.5$, induced power factor $k_h = 1.10$ and ISA/SL conditions (for density ρ).

3. Calculate cruise power using Eq. 20.

   The aircraft weight W varies due to fuel burn (except for batteries) but the simple expression with $W = W_{GTO}$ is appropriate for an initial estimate. The lift to drag ratio L/D is a function of cruise speed V_C and this is where the configuration enters sizing. For an initial estimate, L/D can be assumed to lie between a single edgewise rotor and a tiltrotor. Multiple edgewise rotors are expected to provide lower L/D due to greater hub drag. Multiple proprotors can provide lower or higher L/D, with no data at present to support either case. So for this paper, flight test data from the XV-15 will be used (available in public domain), with a technology improvement factor of $10 - 20\%$ to account for potentially lighter rotors and hence thinner wings.

   The variation of L/D for a single edgewise rotor helicopter can be calculated using standard momentum theory (with appropriate corrections). The aircraft drag area (ft^2) is estimated to be the minimum achieved by current helicopters (based on S-76, SA-341 and OH-6A helicopters as proposed by Harris[37])

$$F = k_F \left(\frac{W_{GTO}}{1000}\right)^{2/3} \quad (22)$$

where W_{GTO} is in lb and $k_F = 2.5$

The variation of L/D for a tiltrotor aircraft requires more detailed calculations because of varying nacelle tilt and wing flap deflection with speed. Instead, the XV-15 data for zero nacelle tilt (rotors in full propeller mode) and zero flap deflection can be used. This data, shown in Fig. 21, gives Eq. 23,

where f_T is the technology improvement factor ($f_T = 1.1$ and 1.2 for 10% and 20% improvement from state of the art (dashed lines in Figure 21)).

The cruise speed for minimum P_C/V_C, which by definition is the speed for best range V_{BR} (minimum energy spent per distance traveled), occurs at maximum L/D (Eq. 20). This speed is used for calculating cruise power.

It is assumed that the lift to drag ratio L/D remains constant for a given disk loading; this removes any dependence of L/D on rotor radius, and is perhaps the most lenient (and inaccurate) of all assumptions.

4. Calculate structural weight from statistical trends: $W_S = 0.24\,W_{GTO}$, valid between $3000 - 100,000$ lb gross take-off weight rotorcraft. These new class of aircraft are not expected to follow this trend. But it is a lower bound of current trends and will be a worthwhile target.

5. Calculate power plant weight from weight models given earlier.

$$\begin{aligned} &\text{turboshaft: } W_P = 1.8\,HP_H^{0.9} \\ &\text{battery: } W_P = W_{motor} \\ &\text{fuel cell: } W_P = W_{motor} \end{aligned} \quad (24)$$

HP_H is the hover power in hp. The statistical trend for turboshaft is valid between $300 - 20,000$ engine hp.

Calculate fuel weight from total energy required for the mission.

$$\begin{aligned} &\text{turboshaft: } W_{FUEL} = SFC\ E_{hp-hr} \\ &\text{battery: } W_{FUEL} = W_B \\ &\text{fuel cell:} \\ &W_{FUEL} = W_{H2T} + W_{FuelStack}(1 + f_{OH}) \end{aligned} \quad (25)$$

E_{hp-hr} is the mission energy in hp-hr. A SFC of 0.4 lb / hp-hr is assumed. f_{OH} is the 15% weight overhead associated with the fuel stack used in the experimental setup of this paper. Note that while the fuel stack is not an expendable fuel mass, it is categorized as fuel weight to provide a fair comparison with the battery.

6. Calculate empty weight: $W_E = (W_P + W_S)/(1 - f_{WO})$. The 'all other' group is estimated as $W_{Oth} = f_{WO}\,W_E$. This groups includes all of the flight controls, hydraulics, electrical and avionics, cabin furnishing, air-conditioning, de-icing (if needed), vibration dampers, and contingency. Typically this group constitutes up to 30% of W_E for modern aircraft, so $f_{WO} = 0.3$.

7. Calculate useful load and payload

$$W_{USE} = W_{GTO} - W_E$$

$$W_{PAY} = W_{USE} - W_{FUEL}$$

and iterate steps 1–6.

7.3. Results of Sizing

The steps listed in the previous section were carried out for a notional mission of 5 minutes hover at 500 kW and 1 hour cruise at 150 mph. This is an elementary mission appropriate for a new power plant so that key trends do not get buried inside the details of start up, shut down, reserves, etc.

The cruise power for edgewise and tiltrotor configurations are shown in Fig. 23. Tiltrotors require lower cruise power due to higher L/D. For the tiltrotor configuration, the cruise speed is set to 150 mph, where the maximum L/D is expected (Fig. 21). The state of the art at this speed is around 7.7 (solid line in Fig. 21). A 20% increase to 9.2 is assumed here (upper dashed line) to account for technology improvements (thinner wings and perhaps many distributed rotors). Figure 23 shows that for the tiltrotor, the cruise power continues to drop with DL; around 25 lb/ft^2, the cruise power is 180 hp. The disk loading is the weight divided by total disk area (of all rotors). As DL increases from $4-30$ lb/ft^2, the power loading, fixed at 6 lb/hp (Fig. 20) means the rotor/s are forced to operate at higher and higher FM. The underlying FM increases from $0.4 - 0.8$ (not shown) assuming no airfoil stall.

Edgewise rotors require significantly higher cruise power. For the edgewise rotor configuration, the cruise speed is set to the best range speed V_{BR} at each disk loading.

$$
\begin{aligned}
L/D &= f_T \; \left(-0.318 + 0.05126\, V_{mph} - 0.0002346\, V_{mph}^2\right) \qquad \text{for } 0 < V_{mph} < 100 \\
L/D &= f_T \; \left(3.47 + 0.01098\, V_{mph} - 0.00009889\, V_{mph}^2\right) \qquad \text{for } 100 < V_{mph} < 135 \\
L/D &= f_T \; \left(4.23 + 0.04589\, V_{mph} - 0.0001538\, V_{mph}^2\right) \qquad \text{for } 135 < V_{mph} < 270
\end{aligned}
\tag{23}
$$

Figures 24– 28 show gross take-off weights and payload weights for a variety of conceptual powerplants. Figure 24 shows the results for a conventional turboshaft engine as well as a fuel cell-battery hybrid power plant. With the maximum power (and mission) specified, a gross take-off weight of 4000 lb requires a DL of around 27 lb/ft^2. The cruise power is then around 173 hp for the tiltrotor (at 150 mph) and 390 hp for the edgewise rotor at its best range speed of 160 mph. For the turboshaft engine, there is no significant difference in payload between the two configurations, because 1 hour is too short a cruise for the tiltrotor to produce the benefit of reduced fuel burn. The engine weight, scaled to maximum hover power, remains the major contributor to the power group. This however is not the case for electric power. The reduced cruise power has a dramatic impact on the feasibility of electric flight; only the tilting proprotor produces a positive payload, so only the tiltrotor configuration is considered henceforth for the electric power plants.

Figure 25 shows the gross takeoff weights and payload weights for a turboshaft, fuel stack, battery, and fuel stack-battery hybrid power plant. These sizing results are based on a two rotor tiltrotor configuration. They use conservative, flight-proven technology electric power components. This includes a battery specific energy of only 150 Wh/kg, a fuel cell specific power of 0.5 kW/kg, and a hydrogen storage weight percent of 5.4%. The battery power plant assumes that the battery is energy limited rather than power limited, and is therefore sized according to its specific energy. The C-rate ζ is then a fallout. The hybrid power plant includes a fuel stack sized to accommodate the prescribed cruise power, as well as a battery portion sized to accommodate the remaining energy for the mission. The results show that for this mission, only the hybrid power plant can barely carry a payload. The weight break-downs for this case at four different disk loadings are shown in Table 8. Fuel cells that provide 0.5 kW/kg specific power still require custom design. The batteries consist of 68 units of 9 cells, each cell rated at (12C) 100 Ah. These are high power cells and will also require custom design.

Figure 26 shows the effects of an improvement in battery technology. It shows that even with a 250 Wh/kg battery, a battery-only power plant is too heavy to accommodate any payload. In contrast, Fig. 27 shows the effects of improvements in fuel cell and hydrogen storage technology. A 7.5% weight fraction is a reasonable value to use for aviation, where boil-off is of lesser concern than in automobiles. Increasing the specific power of a fuel stack to Toyota's reported 2 kW/kg decreases the weight of the power plant significantly, to the point where a fuel cell power plant can carry substantial useful payload.

So, to summarize, a 2-rotor, hybrid, tilting prop aircraft at the target 4000 lb gross weight would carry no useful payload with flight-proven technology. With the cutting-edge technology improvement factors described above, the useful payload increases to 860 lb.

Thus far, the power plants involving batteries have been sized using specific energy, under the assumption that specific power (or C-rate) is not a limiting factor. Figure 28 shows how the payload weight changes if the battery is in fact power limited. A battery's specific power is based on its C-rating, which specifies the maximum discharge current of the battery. The purple line for C-rating 10+ in Fig. 28 is the same as the purple line in Fig. 25 for hybrid W_{PAY}, in which power was not a limiting factor. The other lines in Fig. 28 show a decreasing payload weight because the power plant weight is increased by a larger battery requirement to provide sufficient power for the mission.

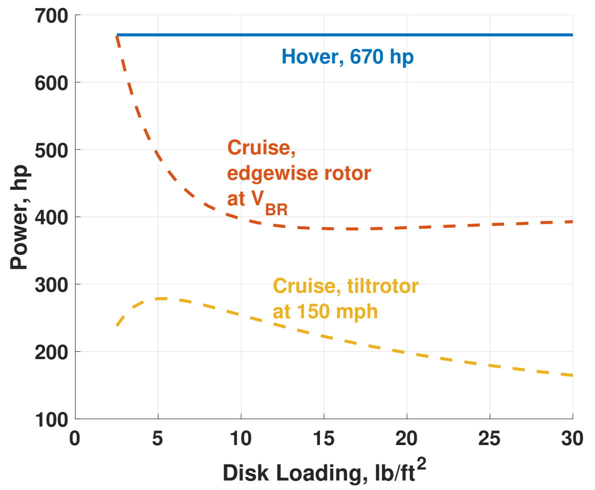

Figure 23: **Cruise power versus disk loading for edgewise and tilting prop rotors.**

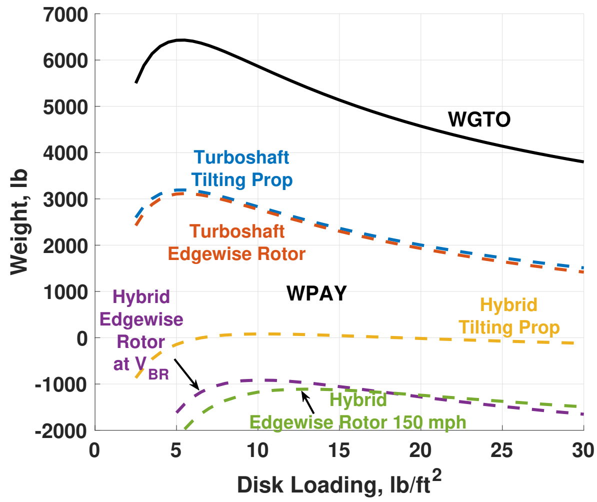

Figure 24: **Payload for edgewise rotor vs tilting proprotor configurations.**

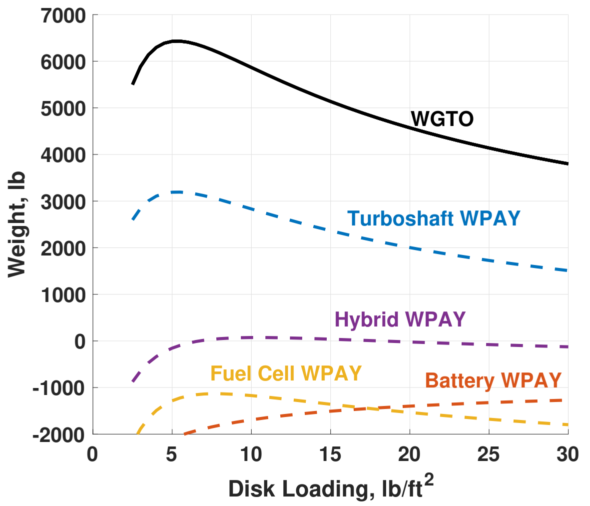

Figure 25: **Payload for tilting proprotor configuration; various power sources; flight-proven technology.**

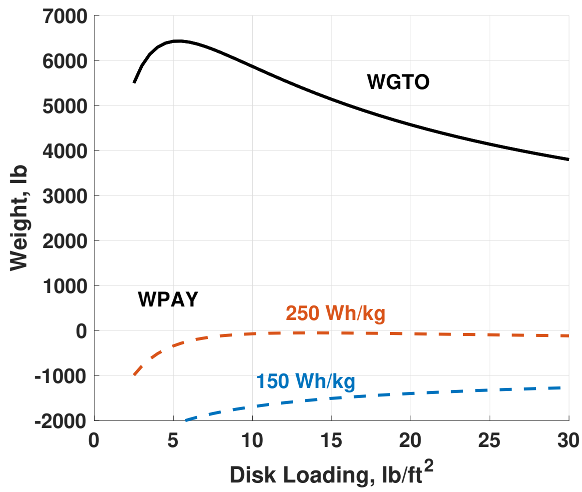

Figure 26: **Battery powered; cutting-edge technology; tilting proprotor.**

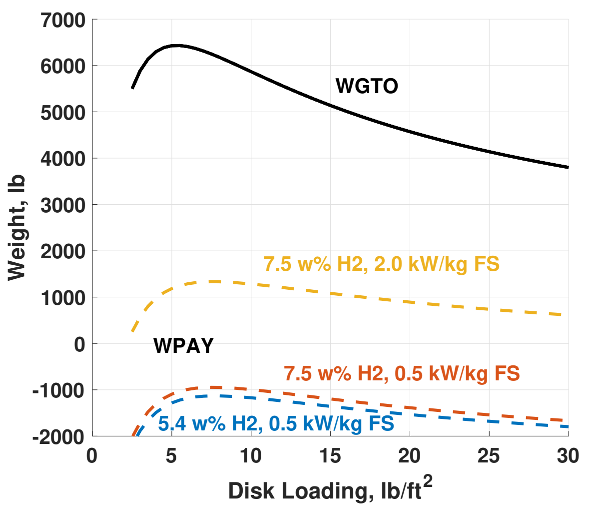

Figure 27: **Fuel cell powered; cutting-edge technology; tilting proprotor.**

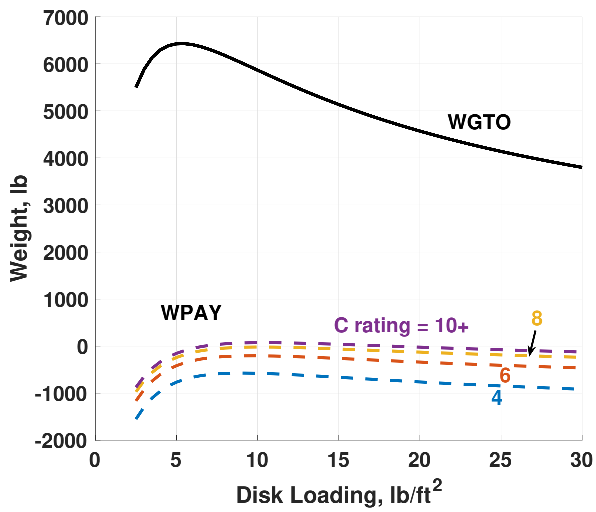

Figure 28: **Fuel cell-battery hybrid powered; flight-proven technology; tilting proprotor.**

Table 8: **Conceptual designs for a tiltrotor aircraft for a 5 min hover, 60 min cruise mission**

Disk loading, lb/ft^2	**10**	**15**	**20**	**27**
W_{GTO}, lb	5866	5136	4571	3994
Rotor radius, ft	9.7	7.4	6.0	4.9
Max hover power, hp	670	670	670	670
Cruise power, hp	255	224	199	174
Cruise speed, mph	150	150	150	150
W_{PAY}, lb	73	38	-23	-98
FUEL:				
W_{FC}, lb	457	400	356	311
PEM Wh/kg	451	451	451	451
PEM kW/kg	0.42	0.42	0.5	0.42
H2 kg	20	17	15	13
Tank w%	5.4	5.4	5.4	5.4
W_{BT}, lb	466	501	530	557
BAT Wh/kg	122	122	122	122
BAT kW/kg	1.46	1.46	1.46	1.46
BAT current in C	12	12	12	12
EMPTY WEIGHT W_E:				
W_P, lb	958	783	679	582
Motors, lb	677	560	485	415
Controller/inverter, lb	135	112	97	83
Cooling, lb	135	112	97	83
W_S, lb	1407	1232	1097	958
W_{Oth}, lb	1010	864	761	660

The results have shown that a hybrid power plant is necessary to sustain the long endurance missions. However, intra-city missions may require only half an hour of cruise (75 mi at 150 mph). The same aircraft sizing was carried out for an abbreviated mission of 5 min hover and 30 min cruise. The resulting payload and gross take-off weights are presented below.

Figure 29 shows that even for this abbreviated mission, the hybrid power plant still allows more payload than batteries or fuel cells alone. For the target gross weight of 4000 lb, the disk loading requirement is 27 lb/ft^2 with a payload of 150 lb. The battery barely breaks even, but is closer to the hybrid than previously seen in the longer mission.

Figure 30 shows the results if the cutting-edge technology improvement factors are used (250 Wh/kg batteries, 7.5 w% storage tanks, and 2.0 kW/kg fuel cells). The payload increases to 1040 lb for the hybrid power plant.

However, as in the previous mission, it is important to note that these results require a battery C-rating of at least 10, as shown in Fig. 31. If the hover time were to decrease to less than 5 min, the C rating for the optimal power plant would increase further. This is because the power required for hover remains the same, while the energy required is decreased. The battery is sized to meet the required energy, so the battery weight required for a shorter hover mission will be smaller. However, since the power required is the same, for this smaller battery to deliver the same power, the C-rating will increase. This C-rating is yet to be achieved for batteries of 150 Wh/kg specific energy, so a comparison of power plant types based on a 6C battery is shown in Fig. 32. The hybrid is no longer significantly lighter than the battery power given this constraint on C-rating.

Based on these results, it is difficult to determine the best design W_{GTO} because although W_{PAY} decreases, total W_{GTO} also decreases. Productivity is a metric used to normalize for this behavior. Productivity is defined as the useful work done per dollar. Useful work is $W_{PAY} \times V_{cruise}$ and cost scales closely with W_E. The expression for productivity is $W_{PAY} \times V_{cruise}/W_E$. Figure 33 shows the productivity of the hybrid power plant for different C-ratings. Based on these results, the optimal eVTOL for this mission would have approximately: a C-rating of 10, disk loading of 11 lb/ft^2, WGTO of 5700, and a payload weight of 430 lb (based on Fig. 31). This is achievable with flight-proven technology fuel cells and batteries, but not with batteries or fuel cells alone. If the cutting-edge technology improvement factors are used, the effect is dramatic – the payload increases to 1570 lb. The greatest impact comes from increasing the fuel cell specific power to 2 kW/kg.

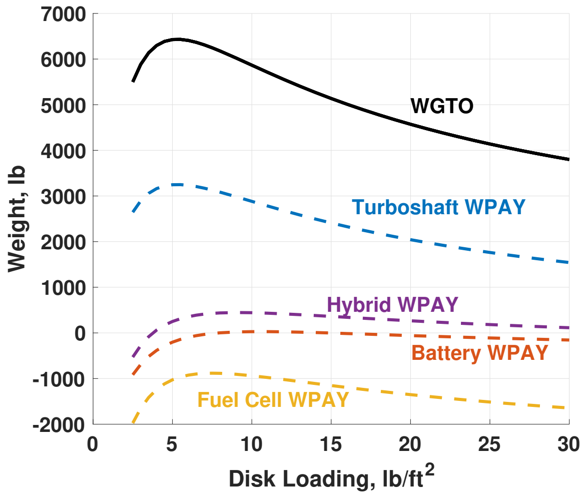

Figure 29: **Various power sources; flight-proven technology; tilting proprotor; mid-length mission.**

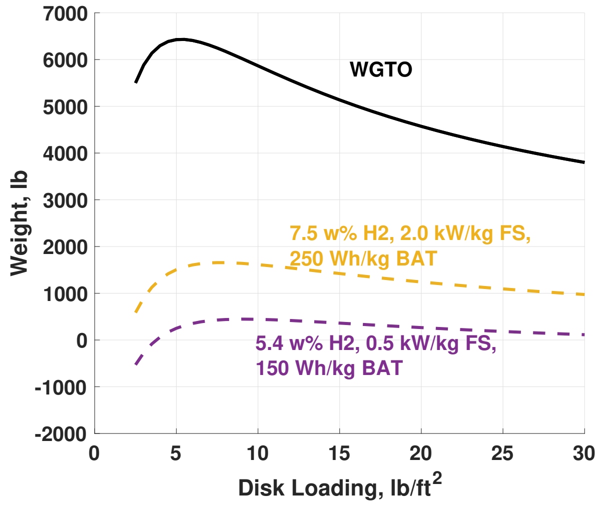

Figure 30: **Fuel cell-battery hybrid power; cutting-edge technology comparison; tilting proprotor; mid-length mission.**

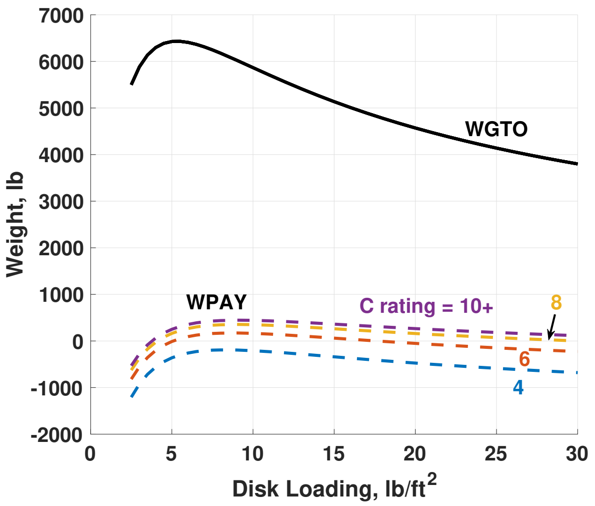

Figure 31: **Fuel cell-battery hybrid; flight-proven technology; tilting proprotor; mid-length mission.**

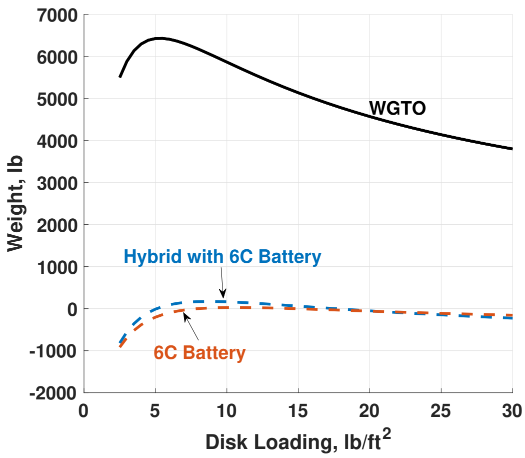

Figure 32: **Fuel cell-battery hybrid versus battery; flight-proven technology; limited battery C-rating; tilting proprotor; mid-length mission.**

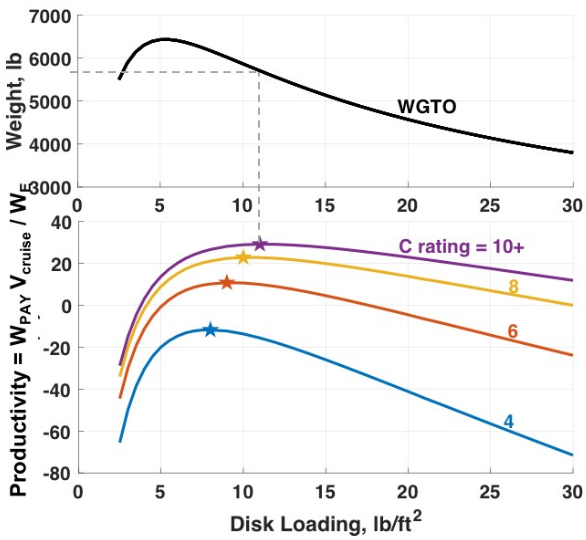

Figure 33: **Productivity for combined fuel cell and battery power plant; flight-proven technology; tilting proprotor; mid-length mission.**

The final mission is the shortest: 5 min hover and 15 min cruise, capable of covering 38 mi at 150 mph, which is barely sufficient for an intra-city commute.

Figure 34 shows the W_{PAY} of different power configurations for a variety of disk loadings. For this mission, the battery-only power is best. This is because less energy is required for the mission, and a relatively large portion of it is at high power, so there is limited payoff for the high energy hydrogen fuel. Furthermore, aside from weight considerations, the combined system also introduces more complexity, not worth the marginal gain in payload. For a target gross weight of 4000 lb, the battery-only system can carry a payload of 490 lb. Accounting for cutting-edge technology improvement factors (250 Wh/kg batteries, 7.5 w% storage tanks, and 2.0 kW/kg fuel cells), the hybrid configuration becomes slightly favorable. The 4000 lb vehicle is then able to carry a 1130 lb payload with a hybrid power plant (plot not shown).

Figure 35 shows how an improvement in battery specific energy to 250 Wh/kg would change the aircraft payload. The fuel stack technology improvement results are identical to that of the longer mission, shown in Fig. 27, because the fuel stack is sized to the maximum power, which remains the same for the abbreviated mission.

For this shortest mission, the battery-only configuration was chosen to investigate the effects of limited C-rating. The results are shown in Fig. 36. A C-rating greater than 3 C, and ideally around 6 C, is still needed for the battery power plant, and greater still for the hybrid.

Figure 37 shows that if the C-rating were limited to 6 C, the battery only configuration would still be preferable to a hybrid configuration.

Figure 38 shows the productivity of the battery-only power for various C-ratings. Based on these results, the optimal aircraft would be battery powered and would have approximately: a C-rating of 6, disk loading of 18 lb/ft^2, W_{GTO} of 4800, and a payload weight of 1100 lb (based on Fig. 36). The hybrid power plant with cutting-edge technology improvement factors at this disk loading could carry a payload of 1780 lb.

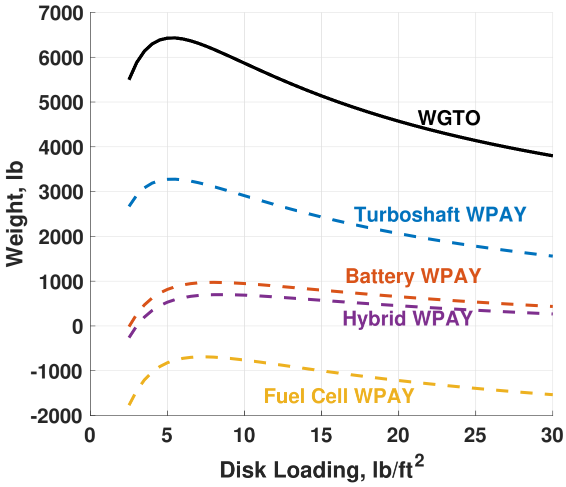

Figure 34: **Various power plants; flight-proven technology; tilting proprotor; shortest intra-city mission.**

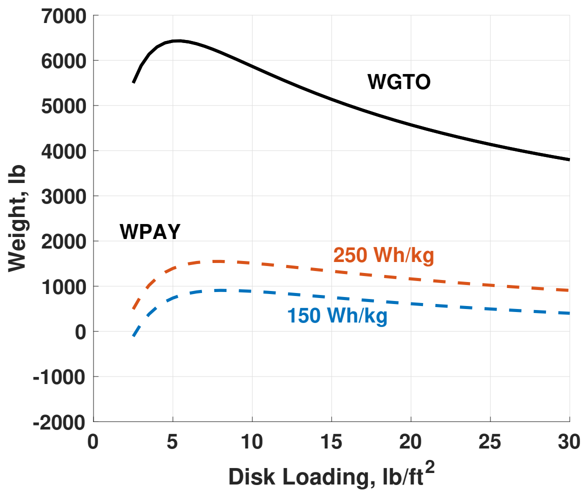

Figure 35: **Battery-only power plant; cutting-edge technology comparison; tilting proprotor; shortest intra-city mission.**

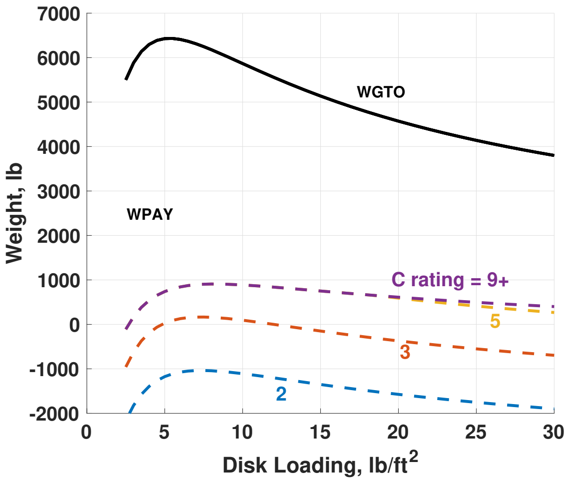

Figure 36: **Battery-only; flight-proven technology; tilting proprotor; shortest intra-city mission.**

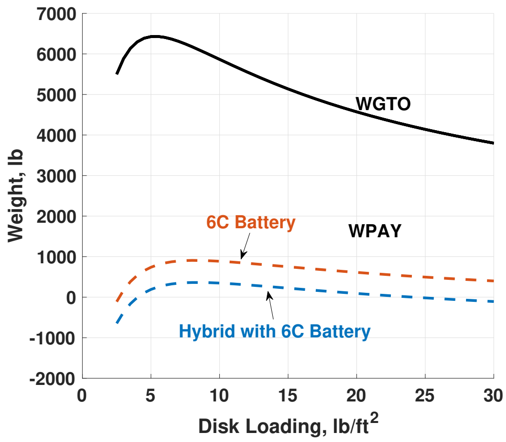

Figure 37: **Fuel cell versus battery; flight-proven technology; limited battery C-rating; tilting proprotor; shortest intra-city mission.**

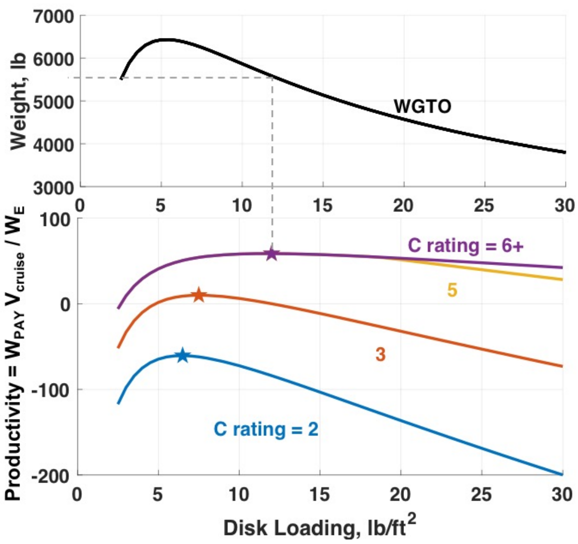

Figure 38: **Productivity of battery-only power; flight-proven technology; tilting proprotor; shortest intra-city mission.**

8. CONCLUSIONS

The use of hydrogen fuel cells combined with Li-ion batteries were examined as a potential candidate to increase range, endurance, and payload of eVTOL aircraft. Based on systematic hardware testing, analytical modeling, and eVTOL sizing, the following key conclusions were drawn:

1. The transient nature of electrochemical sources is primarily driven by a first order capacitative behavior. Battery and fuel cell transients can both be modeled using the same underlying equivalent circuit networks. The circuit elements, and consequently the time constants, are different. There are presently no first principle methods to identify these components easily, so a semi-empirical approach is essential.

2. The models developed in this paper were generally able to capture the magnitudes and waveforms of experimental data. Some mean errors existed for both the fuel stack and battery. Additionally, the fuel stack model failed to capture a transient occurring immediately after it is turned on, and the battery discharge rate model was less accurate when placed in parallel with a fuel stack for flight testing. In general, the voltage model was accurate to within 5% for both the battery and fuel cell.

3. The fuel cells used in this research are in fact faster to respond than batteries, and both are agile enough to handle rapid power transients in VTOL, as long as the current remains in the nominal range. The time constant in the normal operating range for the fuel stack was 0.02 s and for the battery 1.69 s. There are more significant transient behaviors in the low current (high voltage) and high current (low voltage) range that require further investigation. These limits are important for fuel cell eVTOL as they occur near the highest efficiency and highest power limits of the fuel cell.

4. An estimate for the fuel stack balance of plant power losses was found to be 15-25% of operating power. This loss was primarily due to the DC-DC step down, a smaller additional loss associated with the diodes used for power sharing regulation, and a very small loss due to the length of electrical wiring.

5. An estimate for weight overhead of the fuel stack is 15%, again primarily from power electronics. This is the mass that would not be included in the reported specific power of a fuel stack. The value is conservative for this small, low-end fuel stack and step-down.

6. For an inter-city mission of 150 miles in 1 hour, the fuel cell and battery combined power plant is the only option. At this range and speed, using flight-proven technology, a tiltrotor aircraft optimized for productivity (payload weight x speed / empty weight) has a disk loading of 11 lb/ft^2, gross weight of 5700 lb, and a payload of 70 lb.

7. For a mid-length mission of 75 miles in half an hour, a fuel cell and battery combined power plant is the best option. Using flight-proven technology batteries and fuel cells and 10C battery power capability, an aircraft sized for this mission can carry two passengers (400 lb) with a gross weight of 5700 lb and disk loading of 11 lb/ft^2. The battery-fuel cell combination is again superior to either power source alone.

8. For an short intra-city mission of 38 miles in 15 minutes, batteries alone are the lightest power plant option. For this mission, using 6C batteries with flight-proven energy density, a 4000 lb aircraft with a disk loading of 27 lb/ft^2 can carry 480 lb.

9. With present cutting-edge (but not yet flight-proven) technology reported by industry (250 Wh/kg for batteries, 2 kW/kg for fuel cells, and 7.5w% hydrogen storage), an eVTOL can carry four passengers or more for the baseline 150 mile mission. The fuel cell falls barely short of the battery and fuel cell combined power plant, so in general a fuel cell power plant is favorable for its relative simplicity. Maximum productivity for a pure fuel cell powerplant occurs at a W_{GTO} of 5700 lb, a disk loading of 11 lb/ft^2, and W_{PAY} of 1250 lb. For a combined fuel cell and battery power plant, maximum productivity occurs at a W_{GTO} of 5150 lb, a disk loading of 15 lb/ft^2, and W_{PAY} of 1200 lb. A lighter aircraft of 4000 lb gross weight and disk loading of 27 11 lb/ft^2 achieves a W_{PAY} of 680 lb for pure fuel cell and 860 lb for combined fuel cell and battery.

10. Strategic investments for technology development depend on the target mission length. For longer missions (more than 40 mi at 140 mph), cutting-edge (but not yet flight-proven) fuel cell power density is incredibly promising for combined battery and fuel cell power plants. For shorter missions, improving battery energy density for battery power plants is more strategic. For all mission lengths, battery

power density must also be improved to 6-10 C for 150 Wh/kg batteries.

ACKNOWLEDGMENTS

This work is being carried out at the Alfred Gessow Rotorcraft Center, University of Maryland at College Park under the Army/Navy/NASA Vertical Lift Research Center of Excellence (VLRCOE) grant (number W911W61120012), with technical monitoring from Dr. Mahendra Bhagwat and Dr. William Lewis. Additional funding is provided by Army Research Lab, with technical monitoring from Dr. Rajneesh Singh.

8.0.1. Biography

Wanyi Ng grew up in Flagstaff, AZ in the public school system, attended Duke University for her BSE in Mechanical Engineering, and is now at University of Maryland (UMD) getting her MS in Aerospace Engineering. Her research at UMD is in battery and fuel cell power for electric rotorcraft. She is a Pathways Intern at NASA GSFC in Propulsion Engineering, where she worked on the Europa Clipper mission modeling propellant slosh. She is a recipient of Aviation Week's 20 Twenties Award, the Vertical Flight Foundation Scholarship, and UMD's Minta Martin Fellowship. She is a national chapter member of American Institute for Aeronautics and Astronautics (AIAA) and American Helicopter Society (AHS) and is active in UMD's Women in Aeronautics and Astronautics (WIAA) organization.

REFERENCES

[1] Colucci, F., "Lift Where you Need It," *Vertiflite*, Vol. 62, No. 6, November/December 2016, pp. 26–30.

[2] Colucci, F., "AHS Corporate Members," *Vertiflite*, Vol. 62, No. 6, November/December 2016, p. 53.

[3] Whittle, R., "Air Mobility Bonanza Beckons Electric VTOL Developers," *Vertiflite*, Vol. 63, No. 2, March/April 2017, pp. 14–21.

[4] Holden, J., and Goel, N., "Fast-Forwarding to a Future of On-Demand Urban Air Transportation," *UBER Elevate*, October, 2016.

[5] Ng, W., Datta, A., "Development of Propulsion System Models for Electric-VTOL Aircraft," *AIAA Paper 2018-1750*, 1018 AIAA Aerospace Sciences Meeting, AIAA SciTech Forum, January 2018.

[6] Misra, A., "Summary of 2017 NASA Workshop on the Assessment of Advanced Battery Technologies for Aerospace Applications," TR-GRC-E-DAA-TN51429, NASA, 2018.

[7] Lapeña-Rey, N., Mosquera, J., Bataller, E., and Ortí, F., "First Fuel-Cell Manned Aircraft," *Journal of Aircraft*, Vol. 47, No. 6, 2010, pp. 1825–1835.

[8] P. Rathke, J. Kallo, J. Schirmer, T. Stephan, W. Waiblinger, and Weiss-Ungethüm, J., "Antares DLR-H2 Flying Test Bed for Development of Aircraft Fuel Cell Systems P. Rathke," *ECS Transactions*, Vol. 51, No. 1, 2013, pp. 229–241.

[9] Flade, S., Kallo, J., Schirmer, J., and Stephan, T., "Comparison of Anode Configurations During Long Distance Flight in Fuel Cell Powered Aircraft Antares DLR-H2," AIAA Paper 2014. *SciTech Forum 52nd Aerospace Sciences Meeting*, National Harbor, MD, 2014.

[10] Kallo, J., Flade, S., Stephan, T., and Schirmer, J., "Antares DLR H2 - Test Bed for Electric Propulsion," AIAA Paper 2015. *53rd AIAA Aerospace Sciences Meeting*, January, 2015.

[11] Romeo, G., Borello, F., Correa, G., and Cestino, E., "ENFICA-FC: Design of transport aircraft powered by fuel cell & flight test of zero emission 2-seater aircraft powered by fuel cells fueled by hydrogen," *International Journal of Hydrogen Energy*, Vol. 38, No. 1, 2012, pp. 469–479.

[12] Moffitt, B. a., and Zaffou, R., "Polymer-Electrolyte Fuel Cells for UAV Applications Providing Solutions to Revolutionize UAVs," 2012. doi:10.4271/2012-01-2161.

[13] Macewen, R., Seminar, F. C., and Forest, B., "EnergyOr shows off world's first fuel cell multirotor UAV," *Fuel Cells Bulletin*, 2015, April, pp. 5–6.

[14] Datta, A., and Johnson, W., "Requirements for a Hydrogen Powered All-Electric Manned Helicopter," *AIAA Paper 2012-5405*, 12th AIAA ATIO Conference, Indianapolis, IN, 2012.

[15] Sinsay, J. D., Alonso, J. J., Kontinos, D. A., Melton, J. E., and Grabbe, S., "Air Vehicle Design and Technology Considerations for an Electric VTOL Metro-Regional Public Transportation System," *AIAA Paper 2012-5404*, 12-th AIAA ATIO Conference, Indianapolis, IN, 2012.

[16] Nagaraj, V. T., and Chopra, I., "Explorations of Novel Powerplant Architectures for Hybrid Electric Helicopters," *American Helicopter Society 70-th Annual Forum*, Montreal, Canada, 2014.

[17] Snyder, C. A., "Exploring Propulsion System Requirements for More and All-Electric Helicopters," *Paper 2015-20221*, 22nd International Symposium on Air Breathing Engines (ISABE), Phoenix, AZ, 2015.

[18] Dever, T. P., Duffy, K. P., Provenza, A. J., Loyselle, P. L., B., C. B., Morrison, C., and Lowe, A., "Assessment of Technologies for Noncryogenic Hybrid Electric Propulsion," *NASA TP-2015-21658*, 2015.

[19] Datta, A., and Johnson, W., "Powerplant Design and Performance Analysis of a Manned All-Electric Helicopter," *Journal of Propulsion and Power*, Vol. 30, No. 2, February 2014, pp. 490–505.
[20] Johnson, W., "NDARC NASA Design and Analysis of Rotorcraft," *NASA/TP-2015-218751*, 2016.
[21] Matsunaga, M., Fukushima, T., and Ojima, K., "Powertrain System of Honda FCX Clarity Fuel Cell Vehicle," *World Electric Vehicle Journal*, Vol. 3, International Battery, Hybrid and Fuel Cell Electric Vehicle Symposium 24, Stavanger, Norway, 2009.
[22] Hasegawa, T., Imanishi, H., Nada, M., and Ikogi, Y., "Development of the Fuel Cell System in the Mirai FCV," *SAE Technical Paper 2016-01-1185*, SAE 2016 World Congress and Exhibition, Detroit, MI, 2016.
[23] Yoshida, T., and Kojima, K., "Toyota MIRAI Fuel Cell Vehicle and Progress Toward a Future Hydrogen Society," *Electrochemical Society Interface*, Vol. 24, No. 2, Summer 2015, pp. 45–49.
[24] Markel, T., Brooker, A., Hendricks, T., Johnson, V., Kelly, K., Kramer, B., O'Keefe, M., Sprik, S., and Wipke, K., "ADVISOR: a systems analysis tool for advanced vehicle modeling," *Journal of Power Sources*, Vol. 110, No. 2, August 2002, pp. 255–266.
[25] O'Hayre, R., Cha, S., Colella, W., and Prinz, F. B., *Fuel Cell Fundamentals*, 2nd ed., John Wiley and Sons, Inc., 2009.
[26] Yan, Q., Toghiani, H., and Causey, H., "Steady State and Dynamic Performance of Proton Exchange Membrane Fuel Cells (PEMFCs) Under Various Operating Conditions and Load Changes," *Journal of Power Sources*, Vol. 161, May 2006, pp. 492–502.
[27] Yan, Q., Toghiani, H., and Wu, J., "Investigation of water transport through membrane in a PEM fuel cell by water balance experiments," *Journal of Power Sources*, Vol. 158, October 2005, pp. 316–325.
[28] Amphlett, J. C., Mann, R. F., Peppley, B. A., Roberge, P. R., and Rodrigues, A., "A Model Predicting Transient Responses of Proton Exchange Membrane Fuel Cells," *Journal of Power Sources*, Vol. 61, No. 1-2, July-August 1996, pp. 183–188.
[29] Ceraolo, M., Miulli, C., and Pozio, A., "Modelling Static and Dynamic Behavior of Proton Exchange Membrane Fuel Cells on the Basis of Electro-chemical Description," *Journal of Power Sources*, Vol. 113, No. 1, January 2003, pp. 131–144.
[30] Benziger, J., Chia, E., Moxley, J. F., and Kevrekidis, I. G., "The Dynamic Response of PEM Fuel Cells to Changes in Load," *Chemical Engineering Science*, Vol. 60, No. 5, March 2005, pp. 1743–1759.
[31] Ziogou, C., Voutetakis, S., Papadopoulou, S., and Georgiadis, M. C., "Modeling, Simulation and Experimental Validation of a PEM Fuel Cell System," *Computers and Chemical Engineering*, Vol. 35, No. 9, September 2011, pp. 1886–1900.
[32] Gao, L., Liu, S., and Dougal, R. A., "Dynamic Lithium-Ion Battery Model for System Simulation," *IEEE Transactions on Components and Packaging Technologies*, Vol. 25, No. 3, September 2002, pp. 495–505.
[33] Shepherd, C. M., "Design of Primary and Secondary Cells II. An Equation Describing Battery Discharge," *Journal of The Electrochemical Society*, Vol. 112, No. 7, 1965, pp. 657–664.
[34] Dong, T. K., Kirchev, A., Mattera, F., Kowal, J., and Bultel, Y., "Dynamic Modeling of Li-ion Batteries Using an Equivalent Electrical Circuit," *Journal of the Electrochemical Society*, Vol. 158, No. 3, January 2011, pp. 326–336.
[35] McDonald, R. A., "Electric Propulsion Modeling for Conceptual Aircraft Design," *AIAA Paper 2013-0941*, 52nd Aerospace Sciences Meeting, AIAA SciTech Forum, January 2014.
[36] Johnson, W., "NDARC - NASA Design and Analysis of Rotorcraft Validation and Demonstration," *AHS Aeromechanics Specialists Conference*, January 2010.
[37] Harris, F. D., "Introduction to Autogyros, Helicopters, and Other V/STOL Aircraft," *Volume II: Helicopters, NASA/SP-2012-215959*, 2012.